INFORMATION TO USERS

University of Alberta

EFFECT OF VARIABLE MATERIAL PROPERTIES ON PURELY THERMAL

PHASE TRANSFORMATIONS IN SHAPE MEMORY ALLOY WIRES –

MODELING & EXPERIMENTS

by

JULIAN JOYCE AMALRAJ Ⓒ

A thesis submitted to the Faculty of Graduate Studies and Research in partial fulfillment

of the requirements for the degree of MASTER OF SCIENCE

Department of Mechanical Engineering

Edmonton, Alberta

Fall, 1999

The author has granted a non-exclusive licence allowing the National Library of Canada to reproduce, loan, distribute or sell copies of this thesis in microform, paper or electronic formats.

The author retains ownership of the copyright in this thesis. Neither the thesis nor substantial extracts from it may be printed or otherwise reproduced without the author's permission.

L'auteur a accordé une licence non exclusive permettant à la Bibliothèque nationale du Canada de reproduire, prêter, distribuer ou vendre des copies de cette thèse sous la forme de microfiche/film, de reproduction sur papier ou sur format électronique.

L'auteur conserve la propriété du droit d'auteur qui protège cette thèse. Ni la thèse ni des extraits substantiels de celle-ci ne doivent être imprimés ou autrement reproduits sans son autorisation.

0-612-47001-6

Canada

University of Alberta

Library Release Form

Name of Author :   Julian Joyce Amalraj

Title of Project :   Effect of variable material properties on purely thermal phase transformations in shape memory alloy wires – Modeling & Experiments.

Degree: Master of Science

Year This Degree Granted: 1999

Permission is hereby granted to the University of Alberta Library to reproduce single copies of this thesis and to lend or sell such copies for private, scholarly or scientific research purposes only.

The author reserves all other publication and other rights in association with the copyright in the thesis, and except as hereinbefore provided, neither the thesis nor any substantial portion thereof may be printed or otherwise reproduced in any material form whatever without the author's prior written permission.

Julian Joyce Amalraj

#5, 8412 – Millwoods Road NW,

Edmonton, Alberta, Canada - T6K 3B3

Date ...2/7/99...................

University of Alberta

Faculty of Graduate Studies and Research

The undersigned certify that they have read, and recommend to the Faculty of Graduate Studies and Research for acceptance, a thesis entitled "Effect of variable material properties on purely thermal phase transformations in shape memory alloy wires – Modeling & Experiments" submitted by Julian Joyce Amalraj in partial fulfillment of the requirements for the degree of Master of Science.

Dr. A Bhattacharyya (Supervisor)

Dr. M G Faulkner (Supervisor)

Dr. A W Lipsett

Dr. A M Robinson

Date: 30 June 1999

ABSTRACT

In this dissertation, we address the issue of the role of variable material properties in thermally induced phase transformations in shape memory alloy polycrystalline wires. This is done in two main parts. The first part involves modeling the temperature distribution in an SMA wire with variable thermal and electrical properties in the context of a one-dimensional (1-D) boundary value problem where an initially martensitic SMA wire is electrically heated and cooled by convection. The model accounts for an evolution in the thermal conductivity, electrical resistivity and heat capacity during the phase transformation. The evolution in the 1-D temperature field is found by implementing a Galerkin-based finite element method and is used in combination with a recursive iteration scheme to accurately determine the change in the material properties during a time step. This numerical approach is validated by comparing it with a known analytical solution that includes variable thermal properties. A parametric study on the SMA phase transformation indicates that, based on the assumed values for the material properties, the heat capacity is the least important factor that needs to be accounted for, whereas the electrical resistivity is the most important. When predicting the cyclic response of SMA wire actuators, a model that does not account for property variations will predict a considerably different frequency of actuation and total martensitic volume fraction at any given time than what is to be expected with the assumption of constant properties.

The second part of the research deals with the measuring of variations in material properties of an equi-atomic Ni-Ti wire that undergoes a thermally induced phase

transformation. Various experimental procedures are adopted for this purpose that take into account the unique nature of the phase transformation in an SMA wire. Apart from measuring the material properties (i.e. thermal conductivity, electrical resistivity and heat capacity for the two phases), the total heat of transformation, the convection coefficient along the length of the wire and the equivalent convection coefficient at the ends of the wires are also determined. The experiments showed a 100 % change in thermal conductivity, 12.8 % change in resistivity and a 31.3 % change in heat capacity between the two phases of austenite and martensite for the Ni-Ti wire. The resulting simulation of the temperature – time curve and strain – time curve using the measured properties showed good agreement with the experimentally observed thermo-mechanical behavior for this wire. The result also confirmed the conclusions of the parametric studies done in the first part of the research that clearly showed that variations in material properties cannot be ignored during modeling of SMA behavior.

ACKNOWLEDGEMENTS

CONTENTS

3   EXPERIMENTAL   CHARACTERIZATION   OF   NI-TI   WIRE   WITH VARIABLE MATERIAL PROPERTIES

4 CONCLUSIONS AND FUTURE WORK

TABLES

FIGURES

SYMBOLS

θ - - - Temperature.

ξ - - - Martensitic volume fraction.

σ - - - Applied stress.

D - - - Slope of applied stress – transformation temperatures.

K_A - - - Thermal conductivity of SMA in austenite phase.

K_M - - - Thermal conductivity of SMA in martensite phase.

$\rho_{E,M}$ - - - Electrical resistivity of SMA in martensite phase.

$\rho_{E,A}$ - - - Electrical resistivity of SMA in austenite phase.

$C_{V,M}$ - - - Heat capacity of SMA in martensite phase.

$C_{V,A}$ - - - Heat capacity of SMA in austenite phase.

H - - - Total heat of transformation.

J - - - Applied current density.

M_S - - - Martensite start temperature under given applied stress.

M_F - - - Martensite finish temperature under given stress.

M_S^0 - - - Martensite start temperature under zero stress.

M_F^0 - - - Martensite finish temperature under zero stress.

A_S^0 - - - Austenite start temperature under zero stress.

A_F^0 - - - Austenite finish temperature under zero stress.

A_S - - - Austenite start temperature under given applied stress.

A_F - - - Austenite finish temperature under given applied stress.

ξ^* - - - Initial martensitic volume fraction.

$S_{M \to A}$ - - - Standard deviation of the $M \to A$ normal distribution.

$S_{A \to M}$ - - - Standard deviation of the $A \to M$ normal distribution.

θ_{amb} - - - Ambient temperature.

h_L - - - Convection coefficient along the length of the wire.

h_B - - - Equivalent convection coefficient at the ends of the wire.

r - - - Radius of the SMA wire.

L - - - Half − length of the SMA wire.

x - - - Independent spatial variable (distance).

t - - - Independent temporal variable (time).

τ - - - Time increment in FEM scheme.

L_q - - - Length of the qth element in FEM scheme.

ϕ_i^q - - - Element shape function.

A^* - - - Global stiffness matrix in FEM scheme.

$\vec{B}^*$ - - - Thermal Load Vector in FEM scheme.

$\bar{\Theta}$ - - - Nodal temperature vector in FEM scheme.

$\overline{\varepsilon}$ - - - Strain at given time.

$\overline{\xi}$ - - - Total martensitic volume fraction of SMA wire at given time.

$\overline{\varepsilon}_{total}$ - - - Total transformation strain for one cycle of actuation.

$\dot{Q}$ - - - Rate of heat flow into the DSC specimen.

V - - - Volume of SMA sample.

ΔR - - - Measured resistance within specified domain length.

A - - - Area of cross-section of SMA wire.

L_1, L_2 - - - Length of test section for measuring resistance.

1. INTRODUCTION AND LITERATURE REVIEW

1.1 Introduction

Shape memory alloys (SMA) undergo a diffusionless solid-state transformation between a high temperature phase of austenite (A) and a low temperature phase of martensite (M). The phase transformation is strongly dependent on temperature and stress. When a initially austenitic SMA is subjected to mechanical loads (and possibly cooled), the phase transformation to martensite is accompanied by significant length changes to the extent of about 8% in polycrystalline Nickel(Ni) - Titanium(Ti) alloys [Funakubo, 1984]. The significant forces and displacements that result on transformation make SMAs promising candidates for actuators [Giurgiutiu, Chaudhry and Rogers, 1990]. When SMAs are integrated into a structure, the structure becomes capable of sensing and actuation, and are commonly referred to as smart structures [Liang and Rogers, 1991].

The fundamental issue towards the implementation of SMAs in smart structures is their thermomechanical response and its control. The effective control of any SMA actuator ensures proper response and hence the reliability of the structure as a whole. Therefore, it is desirable to have not only a complete constitutive model characterizing the SMA response, but also to have accurate values of the thermomechanical material parameters that go into the model. While the first issue has received significant attention in the literature (see Sec.1.2.2 in this thesis), the second issue has apparently not been as carefully studied. Specifically, it is known that the thermal and electrical properties of the SMA (e.g. thermal conductivity, electrical resistivity and specific heat) are significantly

different in the austenite and the martensite state [Funakubo, 1984; Jackson, Wagner and Wasilewski, 1972]. To the best of our knowledge, the only known work where property variations have been used along with a constitutive model to predict thermal fields in SMA wires during constant stress transformation is that of Benzaoui H, Lexcellent C, Chaillet N, Lang B and Bourjault A, (1997). Moreover Benzaoui et al. (1997) have only accounted for electrical resistivity variations and while their comparison between theory and experiment is qualitatively accurate, the quantitative comparison has room for improvement. Determination of the aforementioned properties becomes a tricky issue for SMAs. For example, a non-uniform thermal field in a SMA wire will lead to a non-uniform material state (even though the initial state may be uniform). In that context, experimental procedures need to be developed that can take this inhomogeneous material state into account and provide a way to accurately determine the material properties of the SMA in the purely austenite and the martensite phase. Benzaoui et.al (1997) have not explained as to how they determine the electrical resistivity of the constituent phases. Another option is to take the material properties provided by the manufacturer at their face value and incorporate them into a constitutive model. Such an approach may be risky for two reasons:

1. The manufacturer usually provides single values. They do not consider property variations and neither do they report the percentage error in measurements of the properties.

2. Manufacturers usually provide property values for bulk materials. As material properties of SMAs are very sensitive to alloying elements and processing conditions

[Funakubo, 1984], the data provided by the manufacturer, even if accurate, may not be relevant for a specific SMA geometry (e.g. wires).

Based on these observations:

1. It is necessary to develop a computational approach that can account for all property variations in SMAs, and

2. It is necessary to develop experimental procedures that can accurately determine material properties of SMA wires.

In this dissertation, we address the issue of characterizing the one-dimensional (1-D) temperature field of an SMA undergoing a thermal phase transformation (at constant stress), and examine the effects on the temperature field due to an evolution in the thermal and electrical properties of the SMA. This work has a computational and an experimental component. In the first component, a one dimensional boundary value problem is considered wherein a model of an SMA wire is heated electrically and cooled by convection under zero stress. The following three boundary conditions at the ends of the wire are considered: 1) Adiabatic boundary condition, 2) Isothermal boundary condition, and 3) Convectional boundary condition. The 1-D temperature field in the wire is simulated by discretization in the context of a Galerkin-based finite element method and an evolution in all thermal and electrical properties is accounted for. These properties at each continuum point are taken to be linearly proportional to the martensite volume fraction at that point. The evolution of the martensite volume fraction with the temperature field is implemented using the phenomenological constitutive model suggested by Lagoudas, Bo and Bhattacharyya (1996) which has its origin in the thermodynamic model proposed by Boyd and Lagoudas (1996a, b). A non-uniform

spatial grid is used to account for sharp temperature gradients at the end of the wire and since the material properties evolve during the phase transformation, a recursive iteration procedure is implemented within each time step. The accuracy of the numerical approach is assessed by its prediction of a known analytical solution where the thermal conductivity and heat capacity change with temperature, but the thermal diffusivity (ratio of the thermal conductivity to heat capacity) is held constant [Carslaw and Jaeger, 1959]. Parametric studies are then carried out using material property values reported in the literature.

The second part of this work deals with the experimental characterization of a commercial grade equi-atomic Nickel-Titanium SMA thin wire subjected to constant stress (dia 0.381 mm). The thermal conductivity, electrical resistivity and the heat capacity of the SMA wire in its austenitic and martensitic phases are determined. Based on these measured properties, the computational model is used to predict the temperature - time response and the displacement − time response of the SMA thin wire and is compared with the experimentally measured characteristics.

1.2 Literature review

1.2.1 Background on Shape Memory Alloys

Shape memory alloys have the anthropomorphic qualities of memory and trainability and exhibit what has come to be known as the 'shape memory effect' (SME) in which the alloy has the capability to sense and adapt to an external stimulus. The SME refers to the ability of these alloys to 'remember' and return to their original shape even after rather significant deformations. An initially

austenitic SMA (state 1 in Fig.1-1) may be cooled resulting in a phase transformation to martensite (state 2 in Fig.1-1). At this state, there is no observable length change. When a load is applied, significant deformations (≤ 8 %) are observed as the SMA goes into state 3. These deformations stay in the material on unloading at its low temperature state. The deformation can then be recovered and the material restored to its original shape and size in state 1 by heating.

Experiments with shape memory alloys [Jackson, Wagner and Wasilewski, 1972; Perkins, 1975] show that the above shape memory effect exhibited by these alloys is a solid-solid diffusionless phase transformation. Solid state transformations are basically of two types: 1) Diffusional transformations and 2) Diffusionless or displacive transformations. Diffusional transformations occur due to the motion of atoms over a relatively long distance. In diffusionless (or displacive) transformations, there is no large-scale migration of the atoms over a long distance. Instead the atoms are cooperatively rearranged into a new crystal structure that is more stable for the environment to which the alloy is subjected. Since the transformation is diffusionless, the chemical composition of the parent and product phase is identical. The shape memory effect appears due to a change in crystal structure from the parent phase of austenite to a product phase of martensite by cooling and/or application of stress. Microscopically, the shape memory effect is a result of shearing of atoms (originally in the austenite phase) that results in length changes. For the shape memory effect to occur, the rearranging of atoms must happen in a way called 'twinning' so that the change

of shape due to forward transformation can be fully recovered upon heating. Twinning is described as a process of accommodation of atoms about a mirror plane called as the 'twin boundary' such that the number and type of bonding on both sides are the same. This twin boundary is very mobile due to low energy interfaces and hence can easily be moved by an applied stress while the martensite formation occurs. The resulting martensite is called *'detwinned'* or deformed martensite. Since there are a number of twin boundaries in a shape memory alloy, a very small shear due to lattice accommodation results in a large net shape change that is fully recoverable. A schematic showing the microscopic behavior of atoms exhibiting the shape memory effect is given in Fig.1-2 [Duerig T W and Wayman CM, 1990]. Recovery of the length change and transformation back to the austenite occurs by heating of the alloy and/or removal of the applied stress. This process is fairly repeatable and can be controlled by the stress applied and/or by the temperature of the shape memory alloy. If the transformation is caused by stress, the transformations are referred to as stress-induced phase transformations. If the transformation is caused due to heating (at zero or constant stress), the transformations are referred to as thermally induced phase transformations.

The SME is volume preserving in most shape memory alloys [Bhattacharyya and Kohn, 1995]. The phase transformations are rate-independent in the sense that the amount of the new phase which is formed depends solely on the temperature and stress and not on their rates. Many alloys like Ni-Ti, CuZnAl, CuAlNi and AuCd exhibit this behavior. However, the Ni-Ti alloy is the most preferred in a majority of

applications due to its superior shape memory effect, wide choice in transformation ranges based on composition of the alloy, good structural properties as well as excellent bio-compatibility and corrosion properties. A detailed investigation of the Ni-Ti alloy, its response to stress and temperature changes, its material properties and their evolution was experimentally studied by Jackson etal. (1972) and Funakubo, (1984). Traditionally, SMA wires are the configurations that have been extensively studied and used in many applications like pneumatics, aerospace, vibration control, advanced composites and biomechanics. However in the past decade, different configurations like SMA strips, SMA springs and SMA rods have also been studied and used in a variety of applications.

1.2.2 Constitutive modeling of SMA phase transformations

The constitutive modeling of SMA phase transformations has been quite extensively considered in the literature. The effort can be classified into the following categories;

1) Single crystal approaches [Abeyaratne and Knowles, 1993; Abeyaratne, Chu and James, 1994; Escobar and Clifton, 1994; Bhattacharyya and Kohn, 1995].

2) Micromechanics-based constitutive models [Patoor, Eberhardt and Bervelleir, 1987; Bervelleir, Patoor and Bulsson, 1991; Raniecki and Lexcellent, 1994].

3) Empirical models for control applications [Bo, Kurdila, Lagoudas and Webb,1994; Dickinson, Hughes and Wen, 1996] and

4) Internal variable-based phenomenological constitutive models [Tanaka, 1996; Sato and Tanaka, 1988; Boyd and Lagoudas, 1995].

Different geometrical configurations of SMA actuators have been studied in the past two decades, SMA wires [Miyazaki, Otsuka and Suzuki, 1981; Shaw and Kyriakides, 1995], SMA strips [Lagoudas, Moorthy, Qidwai and Reddy, 1997], SMA rods [Tanaka, Tsukamoto and Tanaka, 1995; Thomson and Griffin, 1993], SMA springs [Liang and Rogers, 1997], and SMA thin films [Wie, Tang and Lee, 1995; Krulevich, Lee, Ramsey, Trevino and Northrup, 1996]. In the case of SMA wire actuators, it is the one-dimensional (1-D) temperature and stress fields that are of interest. Modeling of the 1-D thermomechanical fields in SMA wires has been done by Abeyaratne, Kim and Knowles, 1994; Leo, Shield and Bruno, 1993; Brinson, 1990 and Liang and Rogers, 1990. Detailed modeling of the thermal fields in thermoelectrically actuated SMAs have been reported by Bhattacharyya, Lagoudas, Wang and Kinra (1995). Their work may easily be adapted to study the 1-D thermal fields in any SMA thin wire actuators that include material and cyclic property variations.

1.2.3   Physical properties and their role in phase transformations

A key feature of the phase transformation in shape memory alloys is that all the properties that influence the thermal field, e.g. thermal conductivity, electrical resistivity (relevant when the actuation is induced by electrical heating) and heat capacity are different depending on whether the SMA is in an austenitic or martensitic state. There is then necessarily an evolution in these properties during a phase transformation from austenite to martensite (or vice-versa), as reported by Jackson, Wagner and Wasilewski, (1972) and Funakabo, (1984).

Also accompanying the phase transformation is the evolution or absorption of a significant amount of latent heat as well as the evolution of the heat capacity. This can be measured by using a differential scanning calorimeter (DSC). A small sample of the material is allowed to undergo phase transformation in a DSC, which results in a DSC thermogram. When the sample undergoes a reverse transformation from martensite (M) to austenite (A), the thermogram shows a power peak to represent an endothermic transformation and a power valley to represent an exothermic austenite (A) to martensite (M) transformation. A schematic showing the various stages of a DSC thermogram is given in Fig.1-3 [Shaw & Kyriakides, 1995]. Another vital role of a DSC thermogram is in the determination of the various transformation temperatures that characterize any phase transformation. The $A \rightarrow M$ transformation is characterized by the martensite start temperature M_S, and the martensite finish temperature M_F. The start and finish temperatures for the $M \rightarrow A$ transformation are referred to as A_S and A_F respectively. In this work we investigate the evolution of thermal and electrical material properties and their effects on the temperature field in a SMA wire.
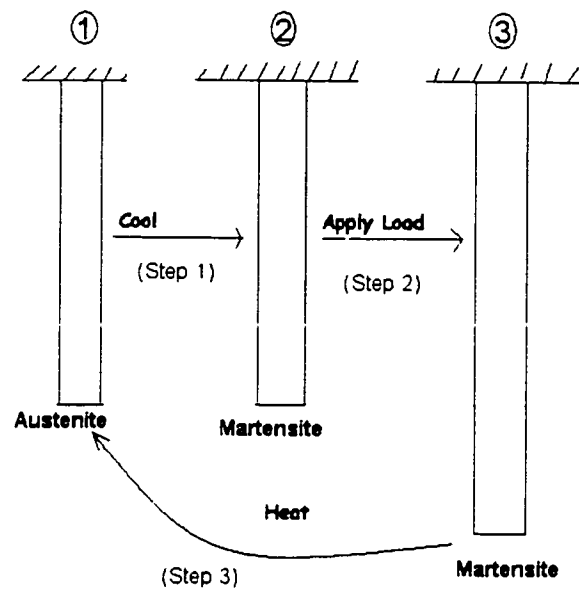
Figure.1.1 Schematic showing macroscopic shape memory effect exhibited by any SMA.
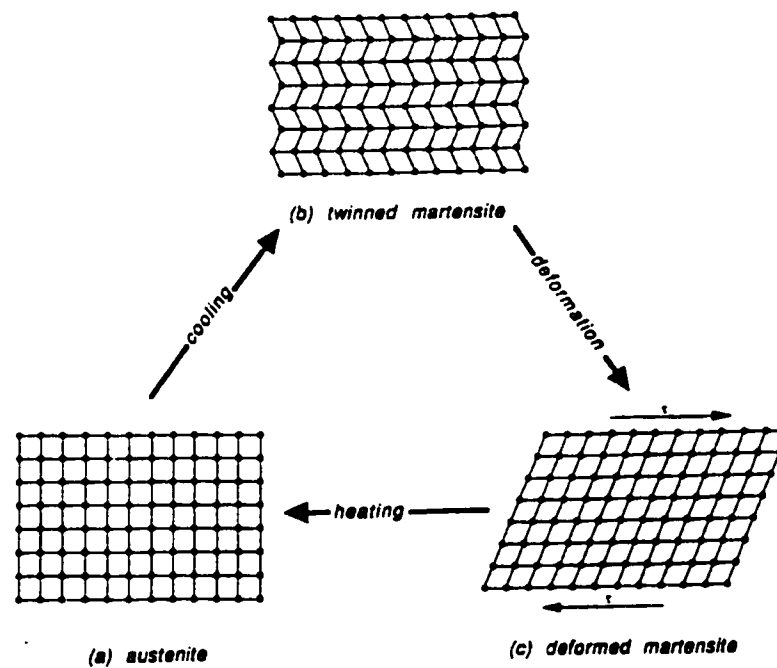
Figure.1.2 Schematic diagram showing microscopic transformations that occur as part of

the Shape Memory Effect [Dureig T W & Wayman C M, 1990].
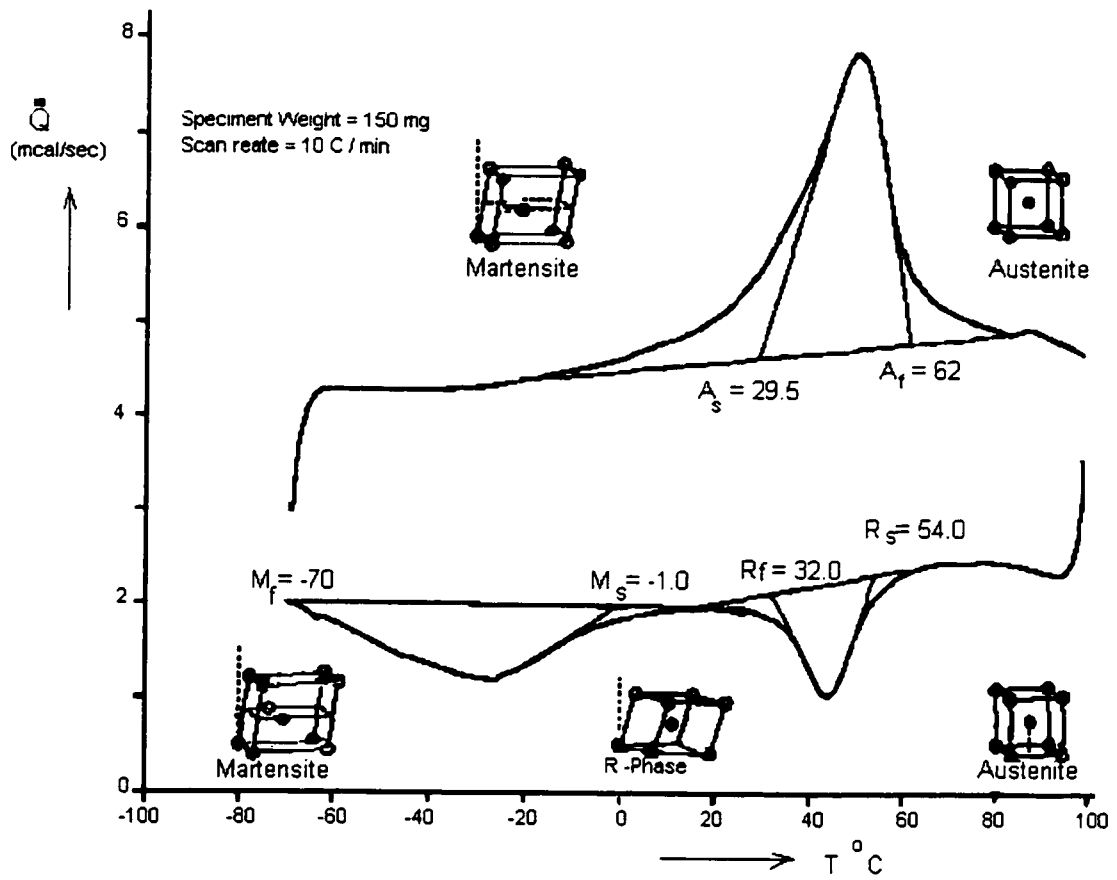
Figure. 1-3 Schematic showing the various stages of a DSC thermogram [Shaw &

Kyriakides, 1995]

2. FINITE ELEMENT MODELING OF PHASE TRANSFORMATIONS IN THIN SMA WIRES WITH VARIABLE MATERIAL PROPERTIES

In this chapter, we report the finite element model of phase transformations in thin SMA wires at zero stress. The model allows for an evolution in material properties including the thermal conductivity, heat capacity and electrical resistivity as the SMA undergoes phase transformation.

2.1 Evolution equations for the thermal and electrical properties of the SMA

The thermal properties, i.e. thermal conductivity (K), heat capacity at constant volume (C_v) and the electrical resistivity (ρ_E) of the SMA are known to change during the course of a phase transformation from austenite (A) to martensite (M) (or vice-versa)[Jackson, Wagner and Wasilewski, (1972) and Funakubo, (1984)]. While Jackson *et al.* (1972) and Funakubo (1984) provide some experimental data on the evolution of the aforementioned properties, the data pertain to Ni-Ti alloys of a different composition than studied experimentally below. As the material properties of these alloys are reported to be quite sensitive to alloy composition [Jackson *et al.* (1972), Funakubo, (1984)], it is felt that evolution equations should be based on experimental data from *alloys with the same composition*. In absence of such data, we assume, for simplicity, that all the thermal and electrical properties of a SMA wire are linearly dependent on the martensitic volume fraction, ξ. As a result

$$K(\xi) = K_A + \xi(K_M - K_A)$$
$$\rho_E(\xi) = \rho_{E.A} + \xi(\rho_{E.M} - \rho_{E.A})$$
$$C_V(\xi) = C_{V.A} + \xi(C_{V.M} - C_{V.A})$$

<div align="right">2-1</div>

where K_j, $\rho_{E.j}$, and $C_{v.j}$ are respectively the thermal conductivity, electrical resistivity and heat capacity of the SMA material when the material is in the jth state ($j = A, M$). If necessary, other more complicated functions may easily be considered.

While the numerical results reported here correspond to a zero stress transformation, we shall present the theory for a constant stress transformation; this will be useful later. For a constant stress transformation, the evolution of the martensite volume fraction, ξ, is taken to be solely dependent on the temperature [Lagoudas et al. (1996)]. The $A \rightarrow M$ transformation starts at the martensite start temperature, M_S, and finishes at the martensite finish temperature, M_F. Both M_S and M_F are sensitive to stress acting on the wire. If 'σ' is the uniaxial stress acting on the wire, then [Liang and Rogers, 1990]

$$M_S = M_S^0 + \frac{\sigma}{D}, \qquad\qquad M_F = M_F^0 + \frac{\sigma}{D}$$

<div align="right">2-1a</div>

where M_S^0 and M_F^0 are known as the *stress-free* $A \rightarrow M$ transformation temperatures. Usually the parameter $D > 0$; thus the effect of tensile stress ($\sigma > 0$) is to cause an increase in M_S and M_F. Based on the above definitions Lagoudas and Bhattacharyya, 1997 proposed the following explicit form of $\xi(\theta)$ given as

$$\xi(\theta) = \xi^* - (1 - \xi^*)\int_{M_S}^{\theta} P(\tilde{\theta})d\tilde{\theta}, \qquad M_F \le \theta \le M_S, \qquad \dot{\theta} < 0, \qquad P(\theta) > 0,$$

<div align="right">2-2</div>

where ξ^* is the martensitic volume fraction at the initiation of the transformation, i.e. $\xi^* = \xi(M_S)$. Eq.2-2 is valid in the temperature range, $M_F \le \theta \le M_S$, and when the

temperature derivative of time is negative, i.e. $\dot{\theta} < 0$. The function $P(\theta)$ is taken to be a normal distribution [Lagoudas and Bhattacharyya, 1997]

$$P(\theta) = \frac{1}{S_{A \to M} \sqrt{2\pi}} \exp\left\{ -\frac{1}{2} \left[\frac{\theta - \frac{1}{2}(M_S + M_F)}{S_{A \to M}} \right]^2 \right\},$$ (2-3)

where $S_{A \to M}$ is the standard deviation of the normal distribution. The value of this parameter may be determined from a differential scanning calorimetric (DSC) measurement of the latent heat evolution [Lagoudas and Bhattacharyya, 1997]. We note that the function $P(\theta)$ satisfies the normalization condition

$$\int_{M_S}^{M_F} P(\tilde{\theta}) d\tilde{\theta} = -1.$$ (2-4)

The $M \to A$ transformation starts at the austenite start temperature, A_S, and finishes at the austenite finish temperature, A_F, defined as

$$A_S = A_S^0 + \frac{\sigma}{D}, \qquad\qquad A_F = A_F^0 + \frac{\sigma}{D}$$ (2-4a)

where A_S^0 and A_F^0 are known as the *stress-free* $M \to A$ transformation temperatures. During this transformation, we have

$$\xi(\theta) = \xi^* - \xi^* \int_{A_S}^{\theta} G(\tilde{\theta}) d\tilde{\theta}, \qquad A_S \leq \theta \leq A_F, \qquad \dot{\theta} > 0, \qquad G(\theta) > 0,$$ (2-5)

where $\xi^* = \xi(A_S)$. The expression, Eq.2-5, is valid in the temperature range, $A_S \leq \theta \leq A_F$ and when the time rate of change of the temperature is positive ($\dot{\theta} > 0$). The function $G(\theta)$ is taken as [Lagoudas and Bhattacharyya, 1997]

$$G(\theta) = \frac{1}{S_{M \to A}\sqrt{2\pi}} \exp\left\{-\frac{1}{2}\left[\frac{\theta - \frac{1}{2}(A_S + A_F)}{S_{M \to A}}\right]^2\right\},$$ 2-6

where $S_{M \to A}$ is the standard deviation of the normal distribution and $G(\theta)$ satisfies the normalization condition

$$\int_{A_S}^{A_F} G(\tilde{\theta})d\tilde{\theta} = 1.$$ 2-7

2.2 The 1-D boundary value problem of a SMA wire actuator

The boundary value problem of a 1-D SMA wire actuator is now developed. The wire is electrically heated and allowed to cool by convection along its length. In this dissertation, we consider thermally induced transformations under constant stress conditions. The ends of the wire are subjected to any of the three boundary conditions: 1. Adiabatic boundary condition, 2. Isothermal boundary condition, and 3. Convective boundary condition. A schematic of the boundary value problem is given in Fig.2-1.

The temperature field in the wire is assumed to be one-dimensional, i.e. $\theta \equiv \theta(x, t)$, where x is the spatial co-ordinate, defined with the origin at the center of the wire, and t is the time. The first law of thermodynamics (conservation of energy) for a 1-D temperature field in a SMA material with variable material properties is given as [Boley and Weiner, 1960; Boyd and Lagoudas, 1996a; Oberaigner, Tanaka and Fischer, 1996]

$$\frac{\partial}{\partial x}\left[K(\xi)\frac{\partial \theta}{\partial x}\right] + \rho_E(\xi)J^2 - \frac{2h_L}{r}[\theta - \theta_{amb}] = C_V(\xi)\frac{\partial \theta}{\partial t} - H\frac{\partial \xi}{\partial t},$$ 2-8

where $K(\xi)$ and $\rho_E(\xi)$ are the thermal conductivity and the electrical resistivity respectively, while J is a constant electric current density in the wire . The convection along the length of the wire is included approximately as a source term [Bhattacharyya *et al.*, 1995] where h_L is the convection coefficient along the length of the wire, r is the radius of the wire and θ_{amb} is the ambient temperature of the environment. The parameter $C_V(\xi)$ is the heat capacity of the SMA material. The parameter H is the magnitude of the latent heat evolved or absorbed per unit volume of SMA material as it undergoes a complete phase transformation from austenite to martensite or vice versa [Bhattacharyya *et al.*, 1995]. Note that the right hand side of Eq.2-8 may be written as

$$
\begin{aligned}
C_V(\xi)\frac{\partial\theta}{\partial t} - H\frac{\partial\xi}{\partial t} &= C_V(\xi)\frac{\partial\theta}{\partial t} - H\frac{\partial\xi}{\partial\theta}\frac{\partial\theta}{\partial t} \\
&= \left[C_V(\xi) - H\frac{\partial\xi}{\partial\theta}\right]\frac{\partial\theta}{\partial t}
\end{aligned}
\tag{2-9}
$$

Using Eqs.2-1 and 2-9, Eq.2-8 can be written as

$$
K(\xi)\frac{\partial^2\theta}{\partial x^2} + (K_M - K_A)\frac{\partial\xi}{\partial\theta}(\theta)\left(\frac{\partial\theta}{\partial x}\right)^2 + \rho_E(\xi)J^2 - \frac{2h_L}{r}[\theta - \theta_{amb}] = \left[C_V(\xi) - H\frac{\partial\xi}{\partial\theta}\right]\frac{\partial\theta}{\partial t}
\tag{2-10}
$$

Eq.2-10 will be utilized in the finite element discretization. Denoting 2L as the total length of the wire, the three symmetric boundary conditions considered are:

(a) Adiabatic boundary condition

$$
\frac{\partial\theta}{\partial x}(\pm L, t) = 0,
\tag{2-11}
$$

(b) <u>Isothermal boundary condition</u>

$$\theta(\pm L, t) = \theta_{amb},$$ 2-12

where θ_{amb} is the ambient temperature of the environment.

(c) <u>Convectional boundary condition</u>

In a realistic situation, the ends of the wire actuator may be attached to grips or supports through which some exchange of heat may occur. For simplicity, the exchange of heat will be taken to depend linearly on the temperature at the ends of the wire, and will be referred as the convective boundary condition for the ends of the wire [Lagoudas and Bhattacharyya, 1998]. Therefore

$$-K(\xi)\frac{\partial\theta}{\partial x}(\pm L, t) = h_B[\theta(\pm L, t) - \theta_{amb}],$$ 2-13

where h_B represents an "effective" convective heat transfer coefficient at the ends of the wire. Note that since the mode of heat transfer to the surroundings along the length of the wire (convection) is fundamentally different from that at its ends (conduction), we use different convection coefficients, h_L (refer Eq.2-8) and h_B (refer Eq.2-13), to highlight the difference.

The initial conditions for the temperature field and the martensitic volume fraction are taken as

$$\theta(x,0) = \theta_{amb} \quad \text{and} \quad \xi(\theta(x,0)) = \xi_{amb}.$$ 2-14

The first of Eq.2-14 assumes that the wire in its initial state is uniformly at the ambient temperature of the environment while the second equation states that the initial state of the material is uniform, and, depending on the value of ξ_{amb}, may be at a purely austenitic state, purely martensitic state or a mixture of both phases.

The boundary value problem as defined by Eq.2-10 subjected to any of the boundary conditions, Eqs.2-11 to 2-13, and the initial conditions of Eq.2-14 is spatially symmetric about the origin. In view of this symmetry, the finite element discretization will only consider a half-length of the wire ($0 \leq x \leq L$). To reflect this symmetry in the 1-D thermal field, the heat flux at $x = 0$ is taken to vanish, i.e.

$$\frac{\partial \theta}{\partial x}(0, t) = 0.$$

<div align="right">2-15</div>

2.3 Galerkin finite element method - based numerical approach

The solution of Eq.2-10 is done using a Galerkin finite element method. The temporal discretization is addressed first, followed by the spatial discretization, and finally the numerical approach is outlined.

2.3.1 The temporal discretization

The temporal discretization is based on a constant time increment, τ. The total time elapsed at the end of the ith time increment is defined as

$$t_i = i\tau, \qquad\qquad i \geq 0,$$

<div align="right">2-16</div>

where i is an integer.

The values of the parameters $\theta(x,t)$ and $\xi(\theta)$ at the end of the ith time increment will be denoted as

$$\theta_i \equiv \theta_i(x) \equiv \theta(x,t_i) \quad \text{and} \quad \xi_i \equiv \xi(\theta_i(x)) \equiv \xi(\theta(x,t_i)) \; . \tag{2-17}$$

Forward differencing is used to define the temporal derivative as

$$\frac{\partial \theta_i}{\partial t} \approx \frac{1}{\tau}[\theta_i - \theta_{i-1}] \; . \tag{2-18}$$

With Eqs.2-17 to 2-18, Eq.2-10 becomes

$$K(\xi_i)\left(\frac{\partial^2 \theta}{\partial x^2}\right)_i + (K_M - K_A)\left(\frac{\partial \xi}{\partial \theta}(\theta)\right)_i \left(\frac{\partial \theta}{\partial x}\right)_i^2 + \rho_E(\xi_i)J^2 - \frac{2h_L}{r}(\theta_i - \theta_{amb})$$
$$= \frac{1}{\tau}\left[C_V(\xi_i) - H\left(\frac{\partial \xi}{\partial \theta}\right)_i\right](\theta_i - \theta_{i-1}) \tag{2-19}$$

In order to facilitate the description of the numerical approach (at the end of this section), Eq.2-19 is written as

$$K(\xi_*)\left(\frac{\partial^2 \theta}{\partial x^2}\right)_i + (K_M - K_A)\frac{\partial \xi}{\partial \theta}(\theta_*)\left(\frac{\partial \theta}{\partial x}\right)_*^2 + \rho_E(\xi_*)J^2 - \frac{2h_L}{r}(\theta_i - \theta_{amb})$$
$$= \frac{1}{\tau}\left[C_V(\xi_*) - H\left(\frac{\partial \xi}{\partial \theta}\right)_*\right](\theta_i - \theta_{i-1}) \tag{2-20}$$

where the " starred " quantities represent an initial guess at the ith time step. We shall return to this issue in Sec.2.3.3.

2.3.2 The spatial discretization

The spatial discretization of Eq.2-20 will be done by the Galerkin-based finite element method whereas a recursive iteration technique will be used to update the values

of the starred quantities within a time step until convergence is achieved. We begin the spatial discretization by weighing Eq.2-20 with a test function, $\gamma(x)$, and writing it in the following weak form

$$\int_0^L K(\xi_*)\gamma(x)\left(\frac{\partial^2\theta}{\partial x^2}\right)_i dx + (K_M - K_A)\int_0^L \frac{\partial\xi}{\partial\theta}(\theta_*)\left(\frac{\partial\theta}{\partial x}\right)_*^2 \gamma(x)dx + J^2\int_0^L \rho_E(\xi_*)\gamma(x)dx$$

$$-\frac{2h_L}{r}\int_0^L (\theta_i - \theta_{amb})\gamma(x)dx = \frac{1}{\tau}\int_0^L \left[C_V(\xi_*) - H\left(\frac{\partial\xi}{\partial\theta}\right)_*\right](\theta_i - \theta_{i-1})\gamma(x)dx \qquad , \qquad 2\text{-}21$$

The half-length of the SMA wire actuator is discretized into N elements as shown in Fig.2-2, where all elements are not necessarily of equal length. The elements are numbered 1 to N, and the nodes are numbered 1 to N+1 from the left to the right. The co-ordinates of the ends of the qth element are x_q and x_{q+1}. Eq.2-21 is now written as a discrete sum by replacing each integral $\int_0^L (\ ) dx$ with the summation $\sum_{q=1}^N \int_{x_q}^{x_{q+1}} (\ ) dx$. For computational simplicity, we assume that the martensitic volume fraction in a particular element is uniform. The uniform martensitic volume fraction in the qth element is defined as

$$\bar{\xi}_i^q = \frac{1}{\Delta L_q}\int_{x_q}^{x_{q+1}} \xi(\theta_i(x))\, dx \ , \qquad 1 \le q \le N \ , \qquad 2\text{-}22$$

where the function $\xi(\theta_i(x))$ follows from either Eq.2-2 or Eq.2-5. The parameter ΔL_q is the length of the qth element, subject to the normalization condition, $\sum_1^N \Delta L_q = L$. In addition, the rate of change of the martensitic volume fraction with temperature in an element is taken to be uniform and is defined as

$$\left(\frac{\overline{\partial\xi}}{\partial\theta}\right)_i^q = \frac{1}{\Delta L_q} \int_{x_q}^{x_{q+1}} \frac{\partial\xi}{\partial\theta}(\theta_i(x))\, dx, \qquad 1 \le q \le N,$$ (2-23)

where $\frac{\partial\xi}{\partial\theta}(\theta_i(x))$ may be determined from either Eq.2-2 or Eq.2-5. With these

definitions, Eq.2-21 becomes

$$\sum_{q=1}^{N} K(\overline{\xi}_*^q) \int_{x_q}^{x_{q+1}} \gamma(x) \left(\frac{\partial^2\theta}{\partial x^2}\right)_i dx + (K_M - K_A) \sum_{q=1}^{N} \left(\frac{\overline{\partial\xi}}{\partial\theta}\right)_*^q \int_{x_q}^{x_{q+1}} \left(\frac{\partial\theta}{\partial x}\right)_*^2 \gamma(x)\, dx$$

$$+ J^2 \sum_{q=1}^{N} \rho_E(\overline{\xi}_*^q) \int_{x_q}^{x_{q+1}} \gamma(x)\, dx - \frac{2h_L}{r} \sum_{q=1}^{N} \int_{x_q}^{x_{q+1}} \left(\theta_i^q - \theta_{amb}\right) \gamma(x)\, dx$$ (2-24)

$$= \frac{1}{\tau} \sum_{q=1}^{N} \left[C_V(\overline{\xi}_*^q) - H\left(\frac{\overline{\partial\xi}}{\partial\theta}\right)_*^q \right] \int_{x_q}^{x_{q+1}} \left(\theta_i^q - \theta_{i-1}^q\right) \gamma(x) dx \qquad \cdot$$

We now define $\theta_i(x)$ as

$$\theta_i(x) = \sum_{j=1}^{2} \theta_i^{q+j-1} \phi_j^q(x), \qquad x_q \le x \le x_{q+1}, \qquad 1 \le q \le N,$$ (2-25)

where $\theta_i^j \equiv \theta_i(x_j)$ is the temperature at the jth node and the ith time step, $\phi_1^q(x)$ and

$\phi_2^q(x)$ are the basis functions, pertaining to the qth element. These are taken as linear

functions

$$\phi_1^q(x) = \frac{x_{q+1} - x}{\Delta L_q} \quad \text{and} \quad \phi_2^q(x) = \frac{x - x_q}{\Delta L_q}, \qquad 1 \le q \le N \qquad \cdot$$ (2-26)

With Eq.2-26, Eq.2-25 is written as

$$\theta_i(x) = [\mathbf{F}]_q^T [\mathbf{\Theta}_e]_i^q, \qquad x_q \le x \le x_{q+1}, \qquad 1 \le q \le N,$$ (2-27)

where $\qquad [\mathbf{F}]_q = \dfrac{1}{\Delta L_q} \begin{Bmatrix} x_{q+1} - x \\ \\ x - x_q \end{Bmatrix}$ $\qquad$ and $\qquad [\mathbf{\Theta_e}]_i^q = \begin{Bmatrix} \theta_i^q \\ \\ \theta_i^{q+1} \end{Bmatrix}$. $\qquad\qquad$ 2-28

In Eq.2-24, $\gamma(x)$ is identified as a two-component vector function with the basis functions (Eq.2-26) as its components. With Eq.2-28, the boundary conditions, Eq.2-15 (at x = 0) and any of the Eqs.2-11 to 2-13 (at x = L) may be used to write Eq.2-24 compactly as

$$\mathbf{A}^* \bar{\Theta}_i = \bar{\mathbf{B}}^* \qquad , \qquad\qquad 2\text{-}29$$

where $\mathbf{A}^*$ is an (N+1)x(N+1) global stiffness matrix, $\bar{\Theta}_i$ and $\bar{\mathbf{B}}^*$ are vectors with N+1 components. The components of $\mathbf{A}^*$ and $\bar{\mathbf{B}}^*$ are given in Appendix A-1. The components of the vector, $\bar{\Theta}_i$, are the nodal temperatures, i.e. $\Theta_i^q = \theta_i^q$. The superscript " * " indicates that the components of $\mathbf{A}^*$ and $\bar{\mathbf{B}}^*$ are a function of the "starred" quantities originally introduced in Eq.2-20. If $\mathbf{A}^*$ and $\bar{\mathbf{B}}^*$ are known, then Eq.2-29 represents a system of linear algebraic equations that may be solved for the nodal temperatures, θ_i^q.

2.3.3 Recursive iteration

The recursive iteration technique to solve for $\bar{\Theta}_i$ (refer Eq.2-29) is outlined. Initially, $\mathbf{A}^*$ and $\bar{\mathbf{B}}^*$ are set equal to their values at the previous time step. i.e. $\mathbf{A}^* = \mathbf{A}^{i-1}$ and $\bar{\mathbf{B}}^* = \bar{\mathbf{B}}^{i-1}$. With these quantities, a trial solution for $\bar{\Theta}_i$ is obtained. With the obtained trial solution, $\mathbf{A}^*$ and $\bar{\mathbf{B}}^*$ are now re-computed, and $\bar{\Theta}_i$ is recalculated. This recursive process continues until the magnitude of the largest change of a nodal temperature from one iteration to the next is less than a small prescribed quantity.

Denoting $\Theta_i^{q,v}$ and $\Theta_i^{q,v+1}$ as trial solutions for the temperature at the qth node obtained from the vth and the $(v+1)^{th}$ iteration respectively, convergence is assumed to have been achieved when

$$\max_{1 \leq q \leq N+1} \left| \theta_i^{q,v+1} - \theta_i^{q,v} \right| \leq \varepsilon \quad , \quad \text{where} \quad \varepsilon \ll 1 \qquad . \qquad \text{2-30}$$

2.4 Numerical results

The numerical approach is validated first by comparison with an analytical solution. The results of a parametric study for a shape memory alloy with variable material properties are then given.

2.4.1 Validation of the numerical approach

We now consider an available analytical solution of a boundary value problem involving temperature-dependent properties [Carslaw and Jaeger, 1959]. A 1-D temperature field is considered in the domain, $0 \leq x \leq L$. The governing equation is taken as

$$\frac{\partial}{\partial x}\left[K(\theta) \frac{\partial \theta}{\partial x}(x,t) \right] + \rho_E J^2 = C_V(\theta) \frac{\partial \theta}{\partial t} \qquad , \qquad \text{2-31}$$

where $\rho_E J^2$ is a time-independent and spatially uniform heat source (due to electrical heating). Note that while $K(\theta)$ and $C_V(\theta)$ are functions of temperature, ρ_E is not. The boundary conditions are

$$\frac{\partial \theta}{\partial x}(0,t) = 0 \qquad \text{and} \qquad \theta(L,t) = \theta_{amb} \qquad . \qquad\qquad 2\text{-}32$$

The initial condition is taken as

$$\theta(x,0) = \theta_{amb} \qquad . \qquad\qquad 2\text{-}33$$

Eqs.2-31 to 2-33 may be converted to a linear problem if $K(\theta)/C_V(\theta)$ is *temperature independent* [Carslaw and Jaeger, 1959]. For simplicity, we take $K(\theta)$ and $C_V(\theta)$ to depend linearly on temperature as

$$K(\theta) = K_0\left[1 + a(\theta - \theta_{amb})\right] \qquad \text{and} \qquad C_V(\theta) = C_V^0\left[1 + a(\theta - \theta_{amb})\right] \qquad , \qquad 2\text{-}34$$

where $K_0 = K(\theta_{amb})$, $C_V^0 = C_V(\theta_{amb})$ and a is a constant parameter. Note that $K(\theta)/C_V(\theta) = K_0/C_V^0$ is temperature independent as required. The temperature field follows from the solution of the following quadratic equation

$$\theta(x,t) + \frac{a}{2}\theta^2(x,t) = Q(x,t) \qquad , \qquad\qquad 2\text{-}35$$

where the negative root of the equation is ignored as it has no physical relevance and $Q(x,t)$ is given as

$$Q(x,t) = \frac{\rho_E J^2}{K_0}\left[L^2 - x^2\right] - \sum_{m=1}^{\infty}\frac{4\sin((m-0.5)\pi)}{L\left((m-0.5)\frac{\pi}{L}\right)^3}e^{-\left(\frac{K_0}{C_V^0}\right)\left[(m-0.5)\frac{\pi}{L}\right]^2 t}\cos\left((m-0.5)\frac{\pi x}{L}\right) \qquad . \qquad 2\text{-}36$$

In the numerical computation, we set $\theta_{amb} = 300$ K. We also take $K_0 = K_M$, $C_V^0 = C_{V,M}$ and $\rho_E = \rho_{E,M}$. The values of these properties and those of J and L are given in Table 2-1. We set the parameter $a = 0.02$ K^{-1}, and compare the predictions of the

analytical solution with those of the present numerical approach using a non-uniform grid of 30 elements and a time step, $\tau = 0.01$. The length of the qth element in the non-uniform grid is

$$\Delta L_q = \begin{cases} 6.0 & , \quad 1 \le q \le 2 \\ 4.0 & , \quad q = 3 \\ 2.0 & , \quad 4 \le q \le 5 \\ 1.0 & , \quad 6 \le q \le 21 \\ 0.5 & , \quad 22 \le q \le 25 \\ 0.4 & , \quad 26 \le q \le 30 \end{cases} \qquad \qquad \text{2-37}$$

The evolution of the temperature profile both temporally and spatially is given in Fig.2-3 and Fig.2-4. The exact values of temperature with time is shown in Table.2-2 for the location, x = 0, as calculated from the analytical solution and our numerical approach. The spatial distribution of the temperature at t = 10 s. calculated by both approaches is also shown in Table.2-3. The difference between the two approaches is less than 0.01% in the worst case.

The role of the spatial and temporal discretization in the numerical predictions of Tables 2-2 and 2-3 are shown in Fig. 2-5 and Fig. 2-6. In Fig. 2-5, all the curves are obtained from the numerical solution using a time step, $\tau = 0.01$ sec, and correspond to the spatial temperature profile at t = 10 sec. Note that only the spatial distribution in the range, $33 \le x \le 40$ mm over which significant temperature gradients are observed is shown. Fig. 2-5 also shows the comparison of a uniform mesh (N = 10), with a non-uniform mesh (N = 20 and N = 30). It is observed that due to the linear nature of the element, the uniform mesh does not yield good convergence for over 20% of the wire. The non-uniform mesh with N = 20 allows for a denser accumulation of elements at the

end of the wire and thus models the temperature distribution more accurately. The "best" simulation of the temperature field is obtained by a non-uniform mesh with N = 30 (element lengths given in Eq.2-37). Fig.2-5 underscores the need to use a non-uniform mesh to accurately capture sharp temperature gradients.

The effect of the temporal discretization with a non-uniform mesh of N = 30 (see Eq.2-37) is shown in Fig.2-6. The difference between the calculated analytical and numerical curves for different time steps is shown and for $\tau = 0.01$ sec, the numerical solution is essentially the same as the analytical solution.

Note that the above results correspond to a value of a = 0.02 (implying an increase in K (θ) and $C_V(\theta)$ with an increase in θ). We have compared the temperature evolution for a = 0.02 with that for a = 0 (constant properties), and have found that the temperature is consistently higher in the latter case. This is the outcome of two reinforcing effects. An increased thermal conductivity improves the ability of the material to conduct heat away from any point and hence lower its temperature (for a > 0). An increased heat capacity implies that a larger amount of heat needs to be stored in order to cause a unit rise in temperature at a continuum point. These effects reinforce each other, resulting in a slower temperature rise.

2.4.2 Parametric studies

In this section, we study a specific boundary value problem of a SMA thin wire initially in the martensitic state, electrically heated and convectively cooled, while it undergoes a M $\rightarrow$ A transformation at zero stress. We evaluate the influence of variable material parameters like thermal conductivity (K), electrical resistivity (ρ_E) and heat

capacity (C_V) when an isothermal boundary condition is assumed at $x = L$. The effect of the three different boundary conditions are then investigated to highlight their role in the evolution of the temperature profile.

Again, due to the symmetry of the problem we will use the half-length of the wire subjected to the boundary condition Eq.2-15 at one end and any of the boundary conditions (Eqs.2-11 to 2-13) at the other end. We take $\theta_{amb} = 300$ K and $\xi_{amb} = 1$. The convection coefficient, h_L, along the wire length is calculated to be 1.4×10^{-4} J/(mm^2.s.K) based on the procedure suggested by Shu, Lagoudas, Hughes and Wen (1997). Refer to Appendix A for detailed calculations. All other parameters are listed in Table.2-1. The standard deviations, $S_{M \to A}$ and $S_{A \to M}$ (Eqs.2-3 and 2-6) are taken as 1.5 K. The time step is taken as $\tau = 0.01$ and the entire wire is discretized using a non-uniform grid (N = 45) where the length of the qth element is given by

$$
\Delta L_q = \begin{cases}
6.0 & , \quad 1 \le q \le 3 \\
4.0 & , \quad 4 \le q \le 5 \\
2.0 & , \quad 6 \le q \le 8 \\
1.0 & , \quad 9 \le q \le 12 \\
0.5 & , \quad 13 \le q \le 16 \\
0.3 & , \quad 17 \le q \le 19 \\
0.1 & , \quad q = 20 \\
0.04 & , \quad 21 \le q \le 45
\end{cases}
\qquad \text{2-38}
$$

Influence of thermal conductivity

The thermal conductivity increases by an order of magnitude during the $M \to A$ transformation (see Table. 2-1). The influence of the thermal conductivity is shown in Fig.2-7, where the temperature evolution has been shown at a position 0.4 mm from the

end (x = 39.6 mm). The top curve corresponds to the temperature evolution when all properties are allowed to evolve whereas the bottom curve corresponds to the situation where all properties except the thermal conductivity are allowed to evolve.

The results indicate that when the thermal conductivity is held constant (the dashed curve) at x = 39.6 mm, the steady state temperature at that point is substantially below the austenitic start temperature, A_S = 345 K. Thus, the material at that point does not undergo the M → A transformation. This is no doubt influenced by the proximity of this location to the isothermal boundary condition at x = 40 mm. However, when the thermal conductivity is allowed to vary (the solid curve in Fig.2-7), the material at x =39.6 mm does go through the M → A transformation. This is due to an evolution in thermal conductivity, as there has been enough heat input at x = 39.6 mm to raise its temperature beyond A_S, despite its proximity to the isothermal boundary condition. This is further explained with Fig.2-8 which is a schematic of three neighboring elements, q-1, q, q+1, where the (q-1)th element has transformed into the austenitic state, the qth element is on the verge of the M → A transformation and the (q+1)th element is in the martensitic state. Since $K_A > K_M$, more heat is conducted into the qth element than out of it, resulting in a net accumulation in the qth element. Had $K_A = K_M$, this extra accumulation would not have occurred. However, with $K_A > K_M$, the qth element can now attain temperatures high enough to undergo the M → A transformation. As can be seen in Fig.2-9, this outcome (due to the evolving thermal conductivity) also happens to narrow the domain over which the isothermal boundary condition suppresses the temperature rise.

Influence of electrical resistivity

The electrical resistivity increases by approximately 24% during the $M \rightarrow A$ transformation (see Table.2-1) and its influence is investigated in Fig.2-10. This suggests that if the electrical resistivity is constant, the resulting temperature rise is slower (bottom curve). As expected, an increase in electrical resistivity results in increased heat generation thereby reducing the transformation time.

Influence of heat capacity

The heat capacity increases by only 11% during a $M \rightarrow A$ transformation (see Table.2-1) and this produces a negligibly small effect (Fig.2-11). The cumulative effect on the temperature evolution when all properties are allowed to change is depicted in Fig.2-12.

Influence of the boundary condition

The effect of the three boundary conditions (when all properties are allowed to vary) is shown in Fig.2-13. Note that we have used $h_B = 9 \times 10^{-4}$ J/(mm^2.s.K) for the convective boundary condition to simulate a relatively high convective heat transfer. It can also clearly be seen that due to an increasing thermal conductivity most regions of the wire have little or no temperature gradients except at the very end ($x = L$).

While the change in the heat capacity has a negligible effect on the temperature evolution, the electrical resistivity and the thermal conductivity have noticeable effects. However, since the major portion of the wire has negligible temperature gradients

($0 \le x \le 32$), the thermal conductivity has a negligible effect in that portion. As a result, when the proposed numerical approach is used to model an experiment on a long wire, the change in the heat capacity is the least important factor to be accounted for while the change in the electrical resistivity is the most important factor of the three.

The impact of the proposed model is most apparent when we address the issue of control of actuators. When an SMA wire is used as an actuator, it is usually the net displacement that is responsible for the actuation and this may be taken to be linearly proportional to the average martensitic volume fraction, as

$$\overline{\xi}(t) = \frac{1}{L} \int_0^L \xi(\theta(x,t)) \ dx \qquad . \qquad 2\text{-}39$$

However, from the control point of view, it is the time evolution of $\overline{\xi}(t)$ that is of interest. Especially when the cyclic response of an actuator is considered, it is convenient to use the net displacement (and thus $\overline{\xi}(t)$) as the control parameter. The frequency of actuation is then decided by the "speed" with which a targeted displacement (and thereby, a targeted $\overline{\xi}(t)$) is achieved. Fig.2-14 gives the evolution of $\overline{\xi}(t)$ vs. t . It is seen that when the model accounts for the change in all thermal properties, the $M \rightarrow A$ transformation (i.e. $\overline{\xi}(t)$ changes from 1 to 0) occurs quicker. In conclusion, a model that does not account for property variations will predict a longer transformation time, and a lower frequency of actuation during a cyclic response of SMA wire actuator than a variable property model would yield.

2.5 Concluding remarks & summary on numerical simulations

We have addressed the issue of modeling the one-dimensional (1-D) temperature field in an SMA wire with variable thermal and electrical properties. This has been done in the context of a 1-D boundary value problem of an SMA wire (initially in an uniform fully martensitic state) heated electrically and subjected to any of the three classical boundary conditions at its ends. The Galerkin finite element method has been used in combination with a recursive iteration technique to address the problem. This approach has been validated by comparison with a known analytical solution. Parametric studies on the SMA phase transformation indicate that the change in the heat capacity is the least important factor to be accounted for and the change in the electrical resistivity is the most important factor. We also conclude that if property variations are not allowed, the model will predict a longer time for a $M \rightarrow A$ transformation than expected, and hence a lower frequency of actuation during the cyclic response of SMA wire actuators.
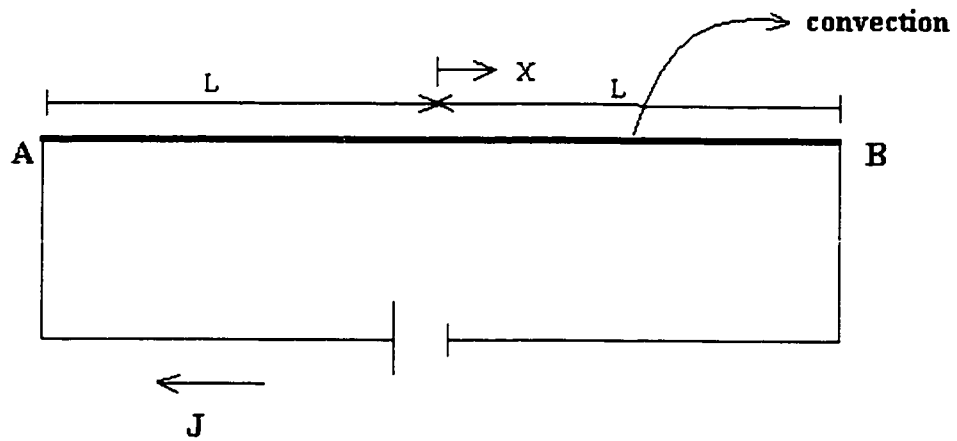
Figure. 2-1 Schematic representation of the 1-D boundary value problem.
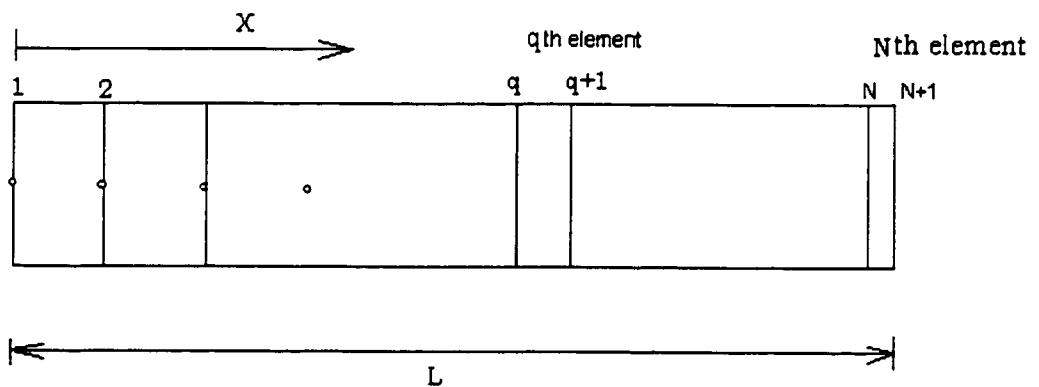
Figure. 2-2 Schematic diagram of the spatial discretization of the 1-D boundary value

problem.
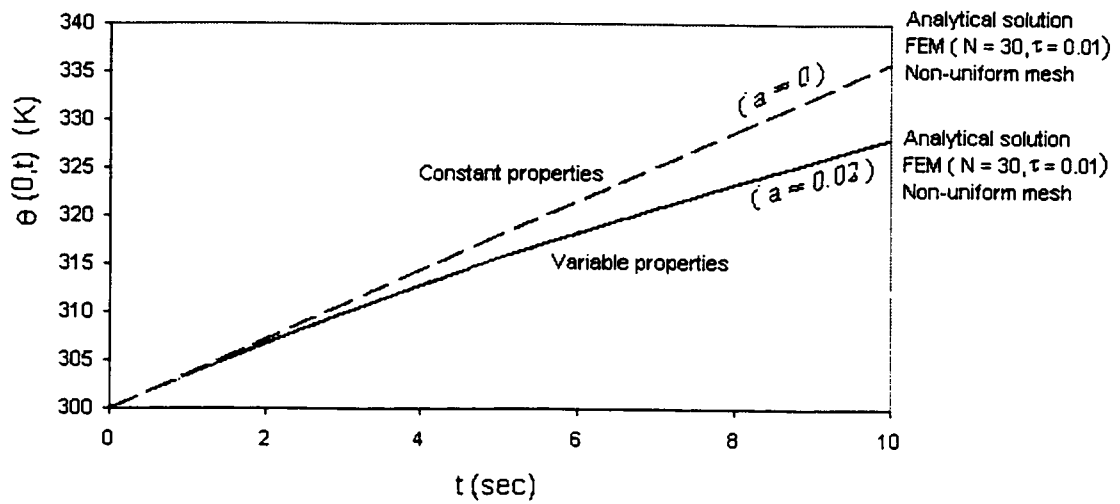
Figure. 2-3 Plot showing the comparison of analytical solution vs finite element results

for temperature profile at the x = 0.
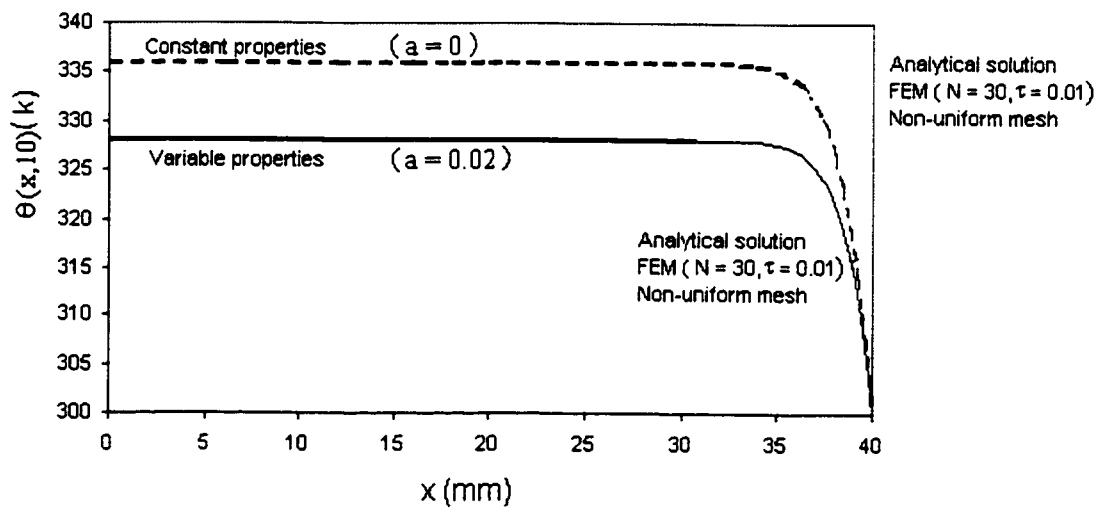
Figure. 2-4 Plot showing the comparison of analytical solution vs finite element results

for spatial temperature distribution at t = 10 s.
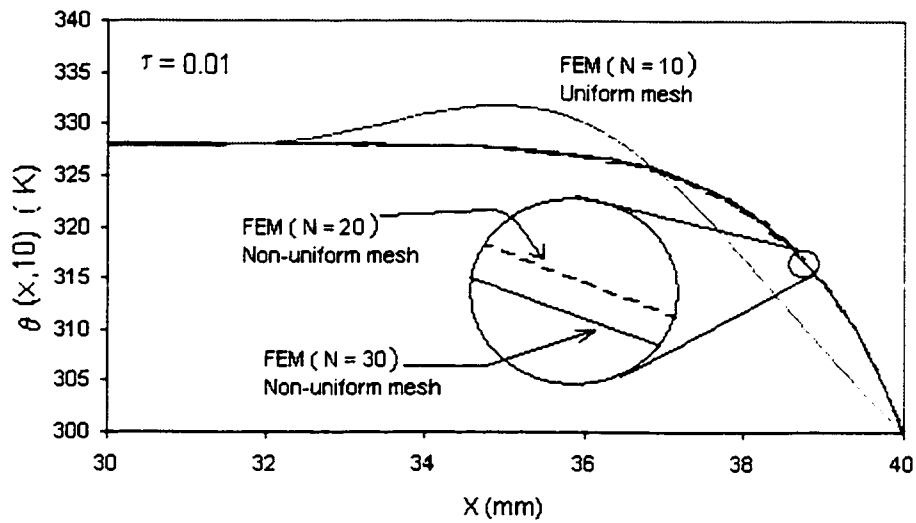
Figure. 2-5 Effect of spatial discretization in the numerical solution when modeling the

temperature distribution at t = 10 s.
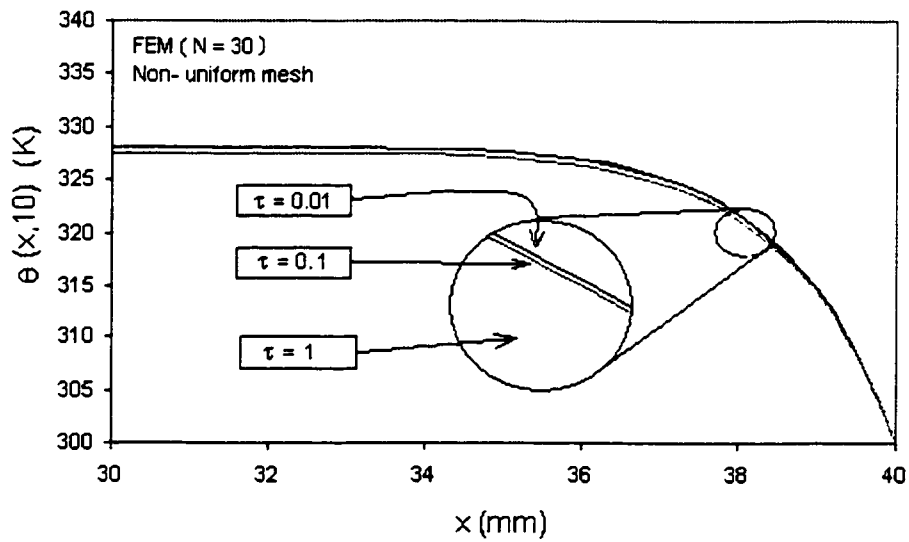
Figure. 2-6 Effect of temporal discretization in the numerical solution when modeling

the temperature distribution at t = 10 s.
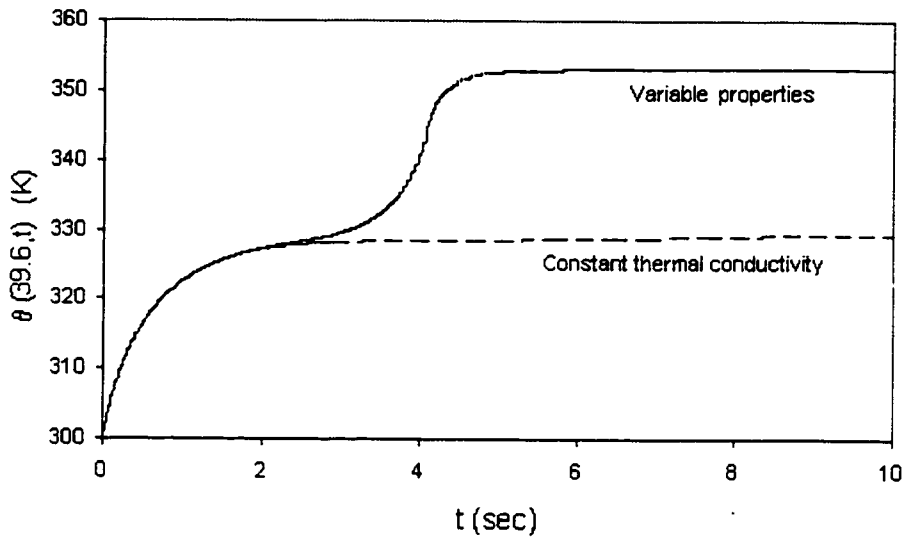
Figure. 2-7 The temperature evolution at x = 39.6 mm. Comparison of numerical

predictions when 1. All properties are allowed to vary; 2. Thermal conductivity is kept

unchanged (all other properties are taken to vary).
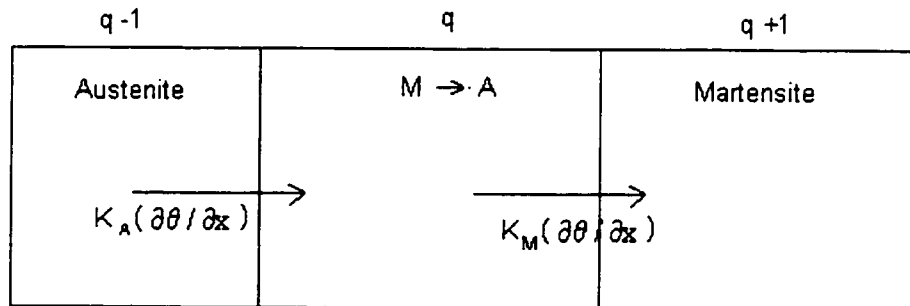
Figure. 2-8 A schematic explaining the effect of thermal conductivity between

neighboring elements.
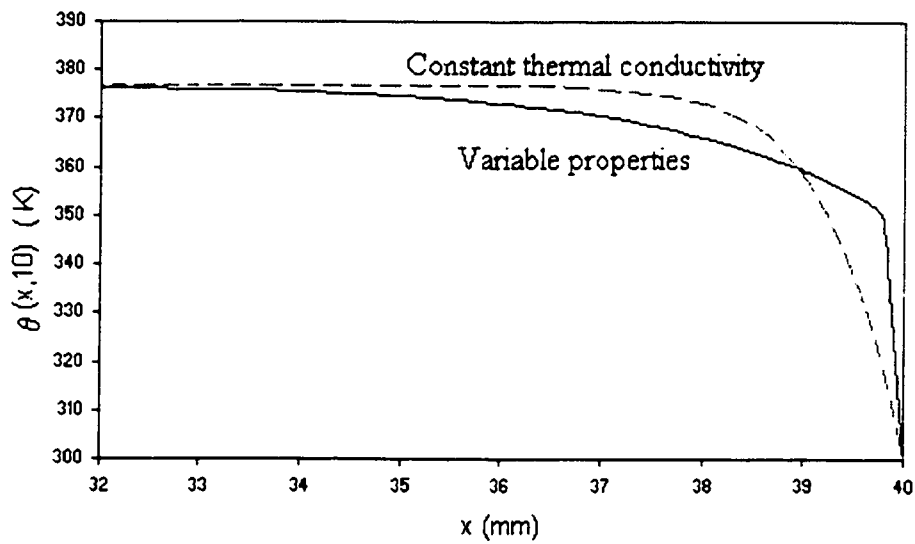
Figure. 2-9 The spatial temperature distribution at t =10 s. Comparison of numerical

predictions when 1. All properties are allowed to vary; 2. Thermal conductivity is kept

unchanged (all other properties are taken to vary).
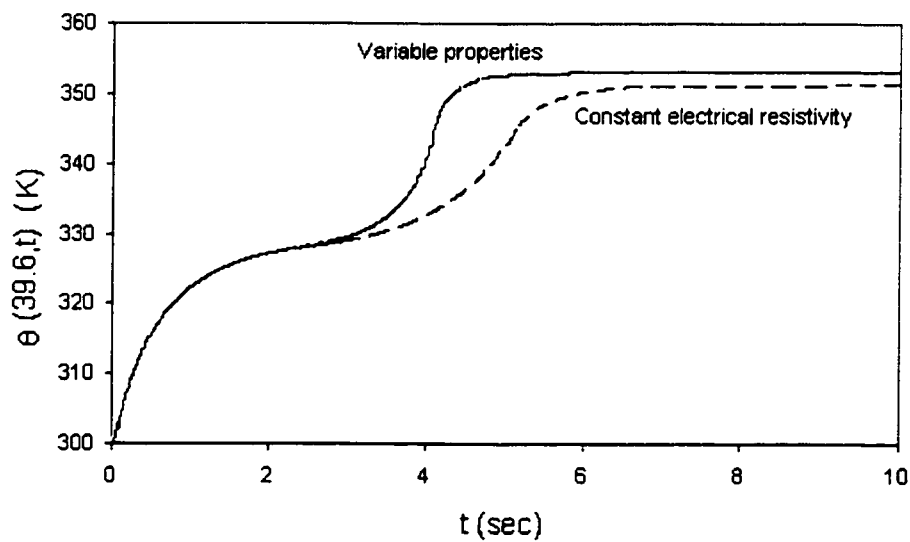
Figure. 2-10 The time-dependent temperature evolution at x = 39.6 mm. Comparison of

numerical predictions when 1. All properties are allowed to vary; 2. Electrical resistivity

is kept unchanged (all other properties are taken to vary).
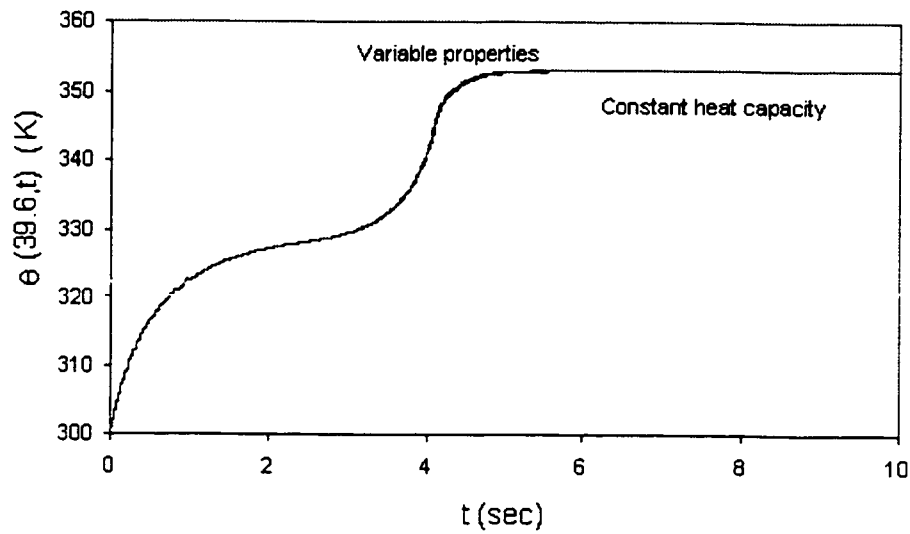
Figure. 2-11 The time-dependent temperature evolution at x = 39.6 mm. Comparison of

numerical approach predictions when 1. All properties are allowed to vary; 2. Heat

capacity is kept unchanged (all other properties are taken to vary).
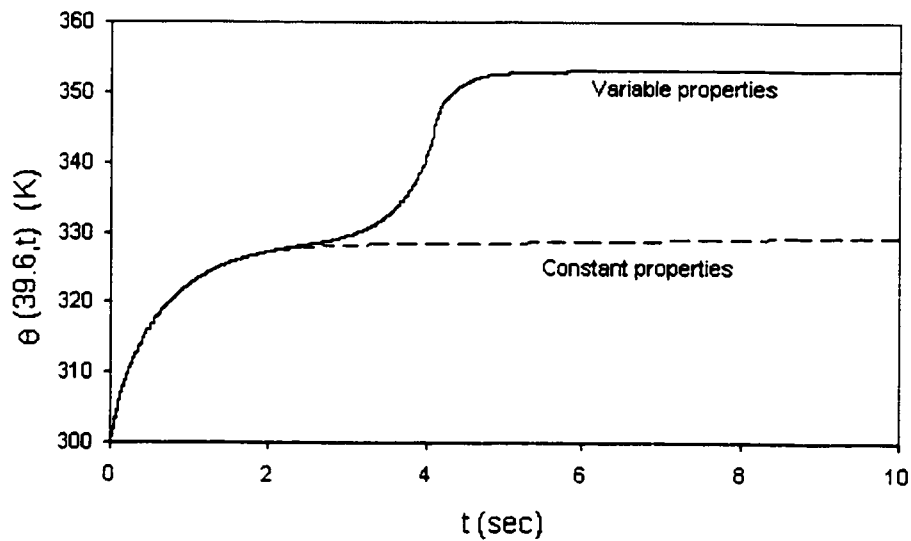
Figure. 2-12 The time-dependent temperature evolution at x = 39.6 mm; Comparison of

numerical predictions when 1. All properties are allowed to vary; 2. All properties are

kept unchanged.
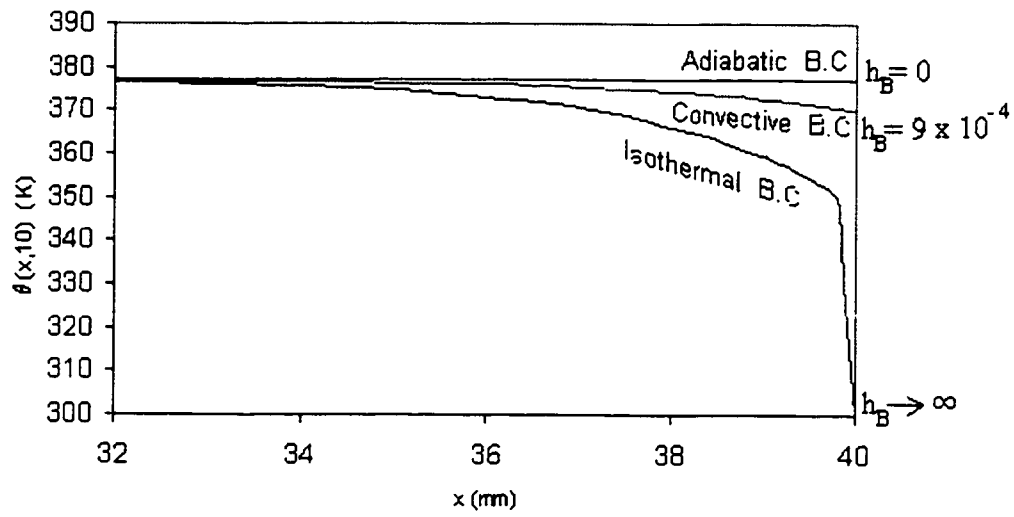
Figure. 2-13   The spatial temperature distribution in the SMA wire at t = 10 s.

Comparison of the three different boundary conditions.
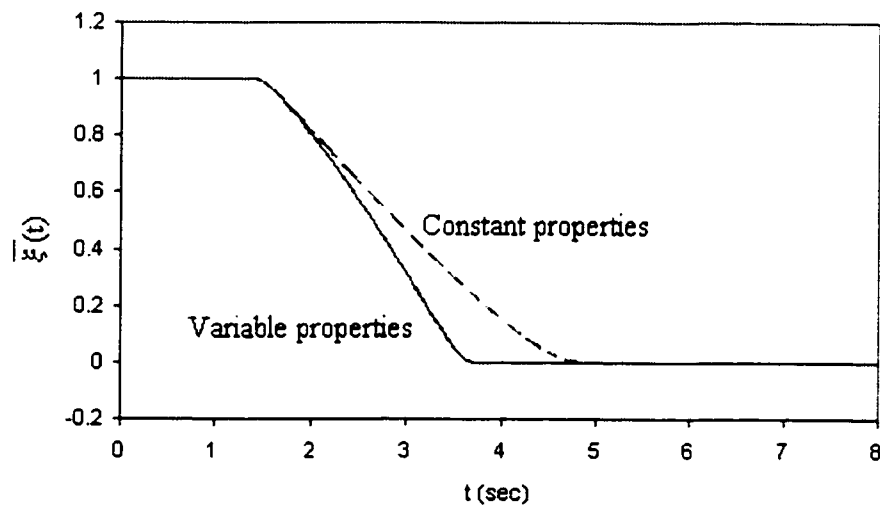
Figure. 2-14   The evolution of the average martensitic volume fraction with time for a

adiabatic boundary condition.

Property (Symbol)	Value	Reference
Thermal Conductivity (K_M)	1.8×10^{-3} J/(mm.s.K)	See footnote 1
Thermal Conductivity (K_A)	1.8×10^{-2} J/(mm.s.K)	Dynalloy, Inc.
Heat Capacity ($C_{V,M}$)	4.861×10^{-3} J/(mm^3.K)	See footnote 1
Heat Capacity ($C_{V,A}$)	5.401×10^{-3} J/(mm^3.K)	Dynalloy, Inc.
Electrical resistivity ($\rho_{E,M}$)	6.993×10^{-4} Ω.mm	Dynalloy, Inc.
Electrical resistivity ($\rho_{E,A}$)	8.693×10^{-4} Ω.mm	Dynalloy, Inc.
Latent heat (H)	0.156 J/mm^3	Dynalloy, Inc.
Convective coefficient (h_L)	1.4×10^{-4} J/(mm^2.s.K)	Shu et. al (1997)
Current density (J)	20 Amps/mm^2	-
Length (L)	40 mm	-
A_S, A_F	345 , 355 deg K	Dynalloy, Inc.
M_S, M_F	322, 332 deg K	Dynalloy, Inc.
Radius of the wire (R)	6.35×10^{-02} mm	Dynalloy, Inc.

Table. 2-1 Values for parameters used in the numerical study.

---

[1] Dynalloy did not provide the value for K_M. However, Fig.71 of Jackson et.al.(1972) shows that K_M is lower than K_A by an order of magnitude. Using the value for K_A given by Dynalloy, we have taken K_M to be smaller by an order of magnitude in this paper. An identical approach is taken for the heat capacity, based on in-house measurements of heat capacity.

t (sec)	θ (0,t) (K)	
	Analytical	Numerical
1.0	303.475	303.474
2.0	306.738	306.736
3.0	309.824	309.821
4.0	312.758	312.755
5.0	315.561	315.557
6.0	318.248	318.245
7.0	320.834	320.830
8.0	323.329	323.325
9.0	325.741	325.737
10.0	328.079	328.075

Table. 2-2 The time-dependent temperature evolution at x = 0; Analytical solution and

numerical solution.

x (mm)	θ (x,10) (K)	
	Analytical	Numerical
0	328.0799	328.075
10	328.0799	328.075
20	328.0799	328.075
30	328.0793	328.075
35	327.6542	327.684
37	325.372	325.308
38	321.7296	321.763
39	312.541	312.478
40	300.000	300.000

Table. 2-3   The spatial temperature profile at t = 10 sec ;   Analytical solution and

numerical solution.

3. EXPERIMENTAL CHARACTERIZATION OF NI-TI WIRES WITH VARIABLE MATERIAL PROPERTIES

3.1 Aim of experiments

The main objective of this part of the research involving experimental characterization of a Ni-Ti thin wire actuator was to develop experimental procedures to determine the thermal and electrical properties of the SMA thin wire in its austenitic and martensitic state. These properties are then used in the finite element model developed in the previous chapter to experimentally predict measured thermal fields in the SMA wire. In order to permit such a comparison, we also need to determine convection coefficients, latent heat of phase transformation and transformation temperatures. The order in which these experiments are reported here is:

1.   Determination of convection coefficient h_B (refer Eq.2-13) for heat conduction through the crimps at the wire ends.

2.   Determination of heat capacities $C_{V,M}$ and $C_{V,A}$ (refer to Eq.2-2), latent heat of phase transformation (i.e. parameter H in Eq.2-8). Since all material properties are found based on experiments during a $M \rightarrow A$ transformation, we also determine the stress-free transformation temperatures A_S^0 and A_F^0 (refer to Eq.2-4a).

3.   Determination of electrical resistivity, $\rho_{E,M}$ and $\rho_{E,A}$ (refer Eq.2-1).

4. Determination of the convection coefficients, h_L (refer to Eq.2-8) for the heat transfer due to convection along the length of the SMA wire.

5. Determination of thermal conductivity, K_A and K_M (refer to Eq.2-2).

3.2 Determination of convection coefficient, h_B

The determination of the convection coefficient h_B (Eq.2-13) is described in this section. An accurate determination of h_B depends on the accuracy of the values of the thermal and electrical properties of the wire. In view of this, the experiment was done with a 0.406 mm diameter nichrome wire (Ni-Cr with a composition of 80-20 at.wt % - Omega Inc.). A nichrome wire was selected as there were reliable values of its thermal and electrical properties reported by the manufacturer. As well, unlike the SMA, the nichrome does not go through a phase change. Since the crimps used at the wire ends are identical to those of the SMA wire, it was assumed that the coefficient, h_B, determined for the nichrome can be used for the SMA wire.

A schematic representation of the setup is given in Fig.3.1. The Ni-Cr specimen of half-length (i.e. L) $\cong 80$ mm ± 1 mm was pinned to Teflon blocks at both ends using steel pins. A mass of approximately 100 grams was attached to one end while the other end was clamped to the structure consisting of a steel bar (dimension 18 x 1.5 x 1.0 inches) and a base plate (dimension 1.5 x 2.0 x 0.2 inches). The purpose of the dead weight was to just hold the wire in place; thus the effects of stress on the nichrome wire specimen is considered to be negligible. Two thermocouples (0.0254 mm dia Type J Iron-Constantan supplied by Omega Inc) were attached at the center and at the right end using a thermal adhesive gel (Loctite 499 thermal cycling gel). The entire apparatus was covered with a

glass and metal box to prevent the effects of local air currents from influencing the temperature measurements. The thermocouples were in turn connected to a DAS-800 A/D board on a computer controlled by in-house software (written in Q-basic) to aid in data collection. The heating of the wire was done electrically using a constant current Hewlett Packard - Harrison 6286A DC power supply (0-20 volts and 0-10 Amperes). In order to monitor applied current, a Fluke 8062A true rms multi-meter (0-2000 mA) with a resolution of ± 0.1 milliamps (mA) was used in series with the power supply as shown (marked 'A' in Fig.3-1). The calibration of the A/D board was done using a Fluke 343A DC voltage calibrator with a resolution of $\pm 5\mu V$. The thermocouples were also calibrated using an ice-bath and water at room temperature as references. A detailed description of the procedure and results of the thermocouple calibration are given in Appendix B.

In order to estimate h_B for the nichrome wire, consider Eq.2-8. Since there is no phase transformation in the nichrome we shall assume (refer to Eq.2-1) that $K_A = K_M = K$, $\rho_{E,A} = \rho_{E,M} = \rho_E$ and $C_{V,A} = C_{V,M} = C_V$; here, k, ρ_E and C_V are the material properties of the nichrome wire. As well, we set $H = 0$ in Eq.2-8 (i.e. no latent heat due to phase transformation). With these simplifications, Eq.2-8 becomes

$$K\frac{\partial^2 \theta}{\partial x^2} + \rho_E J^2 - \frac{2h_L}{r}[\theta - \theta_{amb}] = C_V \frac{\partial \theta}{\partial t} \qquad \text{3-1}$$

along with the end convective boundary condition (Eq.2-13) written as

$$-K\frac{\partial \theta}{\partial x}(\pm L, t) = h_B[\theta(\pm L, t) - \theta_{amb}] \qquad \text{3-2}$$

where we recall that 2L is the total wire length. The solution of Eqs.3-1 and 3-2 yield

$$\theta(x,t) = \theta_S(x) + \theta_t(x,t) \tag{3-3}$$

where $\theta_S(x)$ is the steady state component and $\theta_t(x,t)$ is the transient component of the

total temperature $\theta(x,t)$. The two components are given as

$$\theta_S(x) = \frac{\rho_E J^2 r}{2h_L}\left[1 - Z\left(e^{x\sqrt{A}} + e^{-x\sqrt{A}}\right)\right] + \theta_{amb} \tag{3-4}$$

and $\qquad \theta_t(x,t) = 2\sum_{m=1}^{m=\infty} C_m \cos(\lambda_m x)\, e^{-(A+\lambda_m^2)\frac{k}{C_v}t} \tag{3-5}$

where Z, A, C_m and λ_m are constants given in the Appendix A. In order to determine h_B,

we need to determine h_L (Eq.3-1) for the nichrome wire. This is done by considering the

steady state temperature at $x = 0$. At steady state (i.e. $t \to \infty$), $\theta_t(x,\infty) = 0$ (Eq.3-5).

Therefore, using Eq.3-3, we have $\theta(0,\infty) = \theta_S(0)$, where $\theta_S(0)$ follows from Eq.3-4.

The evolution of the experimentally measured $\theta(0,t)$ is shown in Fig.3-2 for a

current density of 7.8396 Amp/mm^2. It is seen that a reasonable estimation of $\theta_S(0)$ is

the value of $\theta(0,t)$ at $t = 200$ sec, thus $\theta_S(0) = 397.1$ K. With this value in Eq.3-4, h_L can

be determined. Note that Eq.3-4 depends on h_B as well as the nichrome material

parameters listed in Table.3-1. However, numerically $\theta_S(0)$ was found to be insensitive

to the value of h_B over a range $0 \leq x \leq 70$ mm (this is explained subsequently). Thus,

with an arbitrary value of h_B and the experimentally measured $\theta_S(0)$, the solution of

Eq.3-4 yields $h_L = 6.1 \times 10^{-5}$ J/(mm^2.s.K). Fig.3-2 illustrates $\theta(0,t)$ using Eq.3-3 and

compares the experimental results showing exceptionally good agreement. This feature

also indicates that the material property values supplied by the manufacturer are indeed reliable.

The issue as to why $\theta_S(0)$ is insensitive to h_B (or the end boundary condition) can be explained by considering the repetition of the experiment discussed above. During each test, one thermocouple was always kept at x = 0 while the second thermocouple was first kept at x = 65 mm and then at 70 mm (in the previous paragraph, the experiment corresponded to the second thermocouple being at x = 80 mm). The evolution of $\theta(0,t)$ and $\theta(x,t)$ corresponding to the second thermocouple at x = 65, 70, 80 mm are plotted in Fig.3-3. We see that over $0 \le t \le 200$ sec, the temperature evolution at x = 0, 65, 70 mm (top three curves) virtually coincide indicating that there are practically no spatial temperature gradients over $0 \le x \le 70$ mm. Motivated by these observations, a good assumption is that there are no spatial gradients in the vicinity of the center of the wire (i.e. at x = 0). This in turn implies that, at x = 0 mm, $\dfrac{\partial^2\theta}{\partial x^2}(0,t) = 0$ and therefore Eq.3-1 reduces to

$$\rho_E J^2 - \frac{2h_L}{r}[\theta(0,t) - \theta_{amb}] = C_V \frac{\partial\theta}{\partial t}(0,t) \qquad \text{3-6}$$

which is valid at $\theta(0,t)$. Eq.3-6 can be solved for $\theta(0,t)$ and it will necessarily be independent of h_B (or the end boundary condition). Hence we conclude that the evolution of $\theta_S(0)$ is insensitive to h_B.

For the determination of h_B itself, note that the temperature at the end of the wire (x = L) in the steady state will follow from Eq.3-4, i.e. $\theta_S(L)$. The experimentally measured value for $\theta(L,\infty)$ (or $\theta_S(L)$) was taken identical to $\theta(L,t)$ at t = 200 sec. This value was

392.8 K. Eq.3-4 was then used to determine $h_B = 4.5 \times 10^{-4}$ J/(mm^2.s.K). In summary for the nichrome wire,

$$h_L = 6.1 \times 10^{-5} \text{ J/(mm}^2\text{.s.K)} \quad , \quad h_B = 4.5 \times 10^{-4} \text{ J/(mm}^2\text{.s.K)} . \tag{3-7}$$

It is also of interest to discuss the appropriateness of using a convective boundary condition (Eq.3-2) to model the effect of the end grips. The above values of h_L and h_B were used to predict the evolution of $\theta(L, t) - t$ at the end of the wire (L = 80 mm). A comparison of the experimental and theoretical curves in Fig.3-4 indicate that they coincide at t = 250 sec (as they should because we assumed that the experimental $\theta(L,250) \cong \theta(L,\infty)$) and also coincide in the initial transient response $t \le 15$ sec. However, the two curves do not coincide between $15 \le t \le 250$ sec, the maximum difference being about 6-7 ^{0}C in the transient region. This discrepancy suggests that the assumption of a linear boundary condition (Eq.3-2) may not be the most appropriate. Despite this, we use Eq.3-2 as the end boundary condition since it does not appear to influence the thermal field over a major portion of the wire, $0 \le x \le 70$ mm (See discussion earlier in this section). Therefore, for the SMA wire we shall use

$$h_B = 4.5 \times 10^{-4} \text{ J/(mm}^2\text{.s.K)}$$

3.3 Determining Heat capacities ($C_{V,M}$ and $C_{V,A}$), Latent heat of transformation (H) and M → A transformation temperatures

A differential scanning calorimeter (DSC) is used to determine $C_{V,M}$, $C_{V,A}$ (Eq.2-1), the latent heat, H (Eq.2-8) and A_S^0 and A_F^0 (see discussion after Eq.2-4). We first describe the DSC measurement briefly and then elucidate the process of determining the above-mentioned parameters. The evolution of the phase transformation in an SMA sample can be monitored by keeping track of the power supplied at a constant temperature rate using a differential scanning calorimeter (DSC 550 supplied by Instruments Specialist Inc). This instrument consists of a test cell in which two covered aluminum pans (each of with a mass of 22.2 milligrams) are heated simultaneously at a constant temperature rate. One pan contains the test sample and the other pan is kept empty. The difference in the heat input to the two pans is taken equal to the heat input into the SMA sample. Prior to the test with the SMA, the DSC was calibrated using a manufacturer-supplied Indium sample (the details of which are given in Appendix B). For data acquisition a computer was used and for data analysis, the TA-PC ANALYSIS software supplied by the manufacturer was used.

In order to interpret the results, the heat input rate into the SMA sample during heating is taken equal to the heat stored due to a temperature increase rate, $\partial\theta/\partial t$. In the context of the SMA phase transformation, the heat input rate is written as

$$\dot{Q} = \left[C_V(\xi) - H\frac{\partial\xi}{\partial\theta} \right] \frac{\partial\theta}{\partial t} V \qquad\qquad 3\text{-}8$$

where 'V' is the total sample volume. During heating (or the M → A transformation), $\frac{\partial \xi}{\partial \theta}$ follows from Eq.2-5 as $G(\theta)$ (assuming that the SMA at the onset of heating is pure martensite, i.e. $\xi^* = 1$). Therefore Eq.3-8 becomes

$$\dot{Q} = [C_V(\xi) - HG(\theta)]\frac{\partial \theta}{\partial t}V \quad , \quad A_S^0 \le \theta \le A_F^0 \quad , \quad \dot{\theta} > 0 \quad . \qquad \text{3-9}$$

Before the onset of M → A transformation during heating, $C_V(\xi) = C_{V,M}$ and $G(\theta) = 0$. Therefore

$$\dot{Q} = C_{V,M}\frac{\partial \theta}{\partial t}V \quad , \quad \theta < A_S^0 \quad , \quad \dot{\theta} > 0 \quad , \qquad \text{3-10}$$

and after the finish of the M → A transformation, $C_V(\xi) = C_{V,A}$ and again, $G(\theta) = 0$. Therefore

$$\dot{Q} = C_{V,A}\frac{\partial \theta}{\partial t}V \quad , \quad \theta > A_F^0 \quad , \quad \dot{\theta} > 0 \quad . \qquad \text{3-11}$$

DSC measurements are done at a constant temperature rate ($\dot{\theta}$ =constant) and the heat input rate per unit sample volume is reported as a function of temperature. Eq.3-9 is exactly in that form (the right side is solely temperature dependent). Eq.3-9 simplifies to Eqs.3-10 and 3-11 because $C_{V,M}\frac{\partial \theta}{\partial t}V$ and $C_{V,A}\frac{\partial \theta}{\partial t}V$ are assumed independent of temperature. Eqs. 3-9, 3-10 and 3-11 can be used to simulate the entire DSC curve of $\dot{Q}$ Vs θ during heating.

A Ni-Ti SMA sample (weight: 7.3 milligrams of 0.381 mm dia wire) was heated at a constant rate of 2 ^{0}C/min with the $\dot{Q}$ vs θ DSC curve shown in Fig.3-5. The first step

was to determine $C_{V,M}$. This was done at temperatures well below those at which the curve deviates from the baseline. Specifically, since $C_{V,M} = \dot{Q}/(\dot{\theta}V)$ (refer to Eq.3-10), was determined value at three different temperatures ($\theta = 34$, 37, 41 deg C indicated by "x" in Fig.3-5). We took the density of the SMA to be 6.45×10^{-3} g/mm^3 (Dynalloy Inc.), from which the volume was determined as $V = 1.132$ mm^3. At these three temperatures we arrived at $\dot{Q}/(\dot{\theta}V) = 4.2415 \times 10^{-3}$, 4.5066×10^{-3}, 4.7717×10^{-3} J/(mm^3.K) respectively. This indicated that there was a weak temperature dependence of $C_{V,M}$. For simplicity and since the theoretical model assumes that material properties are independent of temperature when the transformation is not taking place, we took $C_{V,M}$ to be the average of these three values; i.e. $C_{V,M} = 4.506 \times 10^{-3}$ J/(mm^3.K). A similar approach was used to determine $C_{V,A}$ where $C_{V,A} = \dot{Q}/(\dot{\theta}V)$ (refer to Eq.3-11). At three different temperatures ($\theta = 76$, 73, 70 deg C indicated by "x" in Fig.3-5) well beyond the completion of transformation, we found $\dot{Q}/(\dot{\theta}V) = 5.832 \times 10^{-3}$, 5.832×10^{-3}, 6.0622×10^{-3} J/(mm^3.K), based on which the average value was found as $C_{V,A}$; i.e. $C_{V,A} = 5.92 \times 10^{-3}$ J/(mm^3.K).

The last step was to determine the latent heat, H (refer to Eq.3-9) and the M $\rightarrow$ A transformation temperatures. Using Eq.3-9, for a specified constant heating rate, $\dot{\theta}$, and volume, V, of the SMA material, $\dot{Q}$ was plotted as a function of θ. In order to be able to plot $\dot{Q}$, several unknown parameters had to be determined: H, A_S^0, A_F^0 and $S_{M \rightarrow A}$ (this last parameter is needed in G(θ), refer to Eq.2-6). These parameters were determined

from the DSC curve in Fig.3-5. While there is a considerable degree of flexibility in the parameter determination, we found that a reasonable simulation was provided by the following combination: $H = 0.125$ J/mm^3, $S_{M \to A} = 0.75$, $A_S^0 = 57.75$, $A_F^0 = 62.75$ as shown in Fig.3-6 where $\dot{Q}/(\dot{\theta}V)$ has been plotted with respect to θ. In summary

$C_{V.M} = 4.506 \times 10^{-3}$ J / mm^{3}K	$C_{V.A} = 5.92 \times 10^{-3}$ J / mm^3.K
$A_S^0 = 57.75$ ^{0}C	$A_F^0 = 62.75$ ^{0}C
$S_{M \to A} = 0.75$	$H = 0.125$ J/mm^3.

3.4 Determination of electrical resistivity

The electrical resistivity, ρ_E, of a wire of length, L and area of cross-section, A, is given as $\rho_E = \dfrac{RA}{L}$ where R is the total electrical resistance of the wire. This relation is valid only when the electrical resistivity is uniform along the wire. However, due to phase transformation, the material state of a SMA wire will be non-uniform along its length. In such a case, the resistivity relation has to be written in the following differential form

$$\frac{dR}{dx} = \frac{\rho_E(\xi)}{A(\xi)} \quad , \quad 0 \le x \le L \quad \quad \text{3-12}$$

where $\rho_E(\xi)$ is the electrical resistivity and $A(\xi)$ is the area of cross-section at a continuum point with martensite volume fraction, ξ. The resistance of a length of the wire in the domain $L_1 \leq x \leq L_2$, is then defined as ΔR and will follow from Eq.3-12 as

$$\Delta R = \int_{L_1}^{L_2} \frac{\rho_E(\xi)}{A(\xi)} dx$$

3-13

If an SMA wire is heated with a constant current of I amps, the voltage drop, ΔV, across the section, $L_1 \leq x \leq L_2$ is given by Ohm's law as

$$\frac{\Delta V}{I} = \Delta R(L_2, L_1) = \int_{L_1}^{L_2} \frac{\rho_E(\xi)}{A(\xi)} dx$$

3-14

Eq.3-14 will be used to determine the electrical resistivity of austenite and martensite. The details of the approach will be given after the experimental setup is described.

The experimental setup shown schematically in Fig.3-7, consists of a Ni-Ti wire (0.381 mm dia) of length 89.4 mm in the martensite state, pinned to Teflon ends and subjected to a constant load of 19.62 N. A thermocouple (0.0254 mm dia Type J Iron-Constantan) was attached at the center of the wire to monitor temperature. The thermocouple was in-turn connected a HP – 7101B strip chart recorder for measuring temperature. The strip chart recorder was used to eliminate high frequency disturbances and noise, which can affect the data collected. A two-probe technique was used to monitor the voltage across a section ($L_1 \leq x \leq L_2$) along the length of the wire and a DC fluke 8062A true RMS multi-meter (0-20 Volts and resolution of $\pm 5mV$) for measuring resistance.

The entire apparatus was covered with a glass and metal box to prevent local air currents and external noise from influencing the measurements. The calibration of the strip chart recorder measuring the voltage of the thermocouple was done using a fluke 343A DC voltage calibrator (resolution of $\pm 5\mu V$). A constant current HP - Harrison 6286A DC power supply (0-20 volts and 0-10 Amperes) was used to heat the wire and a fluke 8062A true RMS multi-meter (0 -2000 mA with a resolution of ± 0.1 mA) was used in series with the power supply to monitor applied current. Detailed calibration procedures for the equipment used in the experiment are given in Appendix B.

To determine $\rho_{E.M}$ (as defined in Eq.2-1), recall that at the ambient temperature, the wire (subjected to a load of 19.62 N) was in the martensitic state. By several experimental trials, it was determined that if the wire was heated with a constant current, $I = 0.5$ amps, the steady state temperature at the center of the wire is 46.5 ^{0}C. This is well below the stress-free austenitic start temperature, $A_S^0 = 57.75$ ^{0}C, determined for the wire in the previous section and ensures that the entire wire is in the martensite phase during the experiments. At this current density a two-probe technique was used to measure the voltage drop across a length $L_1 \le x \le L_2$, of the SMA wire, and the corresponding resistance, ΔR, calculated. Specifically, L_1 was kept fixed at 0 mm (at the crimps on the left end of the wire) and L_2 was changed gradually. Therefore, this measurement not only includes the ΔR defined in Eq.3-14 but also the contact resistance at the crimps (at x = 0 mm). The measured resistance is thus written as

$$R(L_2,0) = \Delta R(L_2,0) + R_{CONTACT} \qquad \text{3-15}$$

where $R(L_2,0)$ as a function of L_2 is plotted in Fig.3-8 for $I = 0.5$ amps. Notice from

Eq.3-14 that if the material state over the range $L_1 \leq x \leq L_2$, of the wire is uniform (say

martensite, i.e. $\xi = 1$), the equation becomes

$$\Delta R(L_2,L_1) = \frac{\rho_{E.M}}{A(1)}(L_2 - L_1)$$

<div align="right">3-16</div>

where $A(1)$ is the cross-sectional area measured in the martensite state. Thus, for a

uniform material state, ΔR is linear in L_2. This is definitely seen to be the case over the

range $35 \leq L_2 \leq 55$ mm (see Fig.3-8). The resistance over this length, $\Delta R(55,35)$,

follows from Eq.3-15 and the absolute values of resistance at the two points ($L_2 = 55$ and

$L_2 = 35$) as $R(55,0) - R(35,0) = 0.1684\ \Omega$. Since $A(1) = \pi r_M^2$ (where the radius

$r_M = 0.1905$ mm), $I = 0.5$ amps and $L_2 - L_1 = 20$ mm, Eq.3-16 gives the martensite

electrical resistivity as $9.603 \times 10^{-4}\ \Omega$mm.

The procedure to determine the electrical resistivity of the austenite was similar. The

wire was heated with a current $I = 1$ Amp such that the steady state temperature at the

center of the wire was $96.0\ ^0C$. This is well beyond the austenite temperature,

$A_F = 72\ ^0C$ calculated by Eq.2-4a (where $A_F^0 = 62.75\ ^0C$, $\sigma = 171$ MPa and $D = 18.49$

MPa/ ^0C). The results of the resistivity measurements are shown in Fig.3-9 for austenite.

In the range, $35 \leq L_2 \leq 55$ mm, the resistance change is again seen to be linear.

Therefore Eq.3-14 can be written as

$$\Delta R(L_2,L_1) = \frac{\rho_{E.A}}{A(0)}(L_2 - L_1)$$

<div align="right">3-17</div>

where A(0) is the area of cross-section in the austenite state. While $L_2 = 35$ and 55 mm,

$\Delta R(55,35) = R(55,0) - R(35,0) = 0.1398 \ \Omega$ and $I = 1$ amp, A(0) needs to be determined.

Note that phase transformation in NiTi SMAs is volume preserving [Funakubo, 1984; Jackson.et al., 1972]; an elemental length $dL(\xi)$ of an SMA wire with cross section area $A(\xi)$ is

$$dV = dL(\xi) \times A(\xi) \qquad , \qquad\qquad 3\text{-}18$$

where dV is independent of ξ. With this condition, we can write

$$dL(0) \times A(0) = dL(1) \times A(1)$$

$$A(0) = \frac{dL(1)}{dL(0)} A(1) = [1 + \varepsilon] A(1) \qquad\qquad 3\text{-}19$$

where $\varepsilon = \dfrac{dL(1) - dL(0)}{dL(0)}$. The parameter ε is the strain introduced in the SMA as it

undergoes a phase change from austenite to martensite. For constant stress thermal transformations, there are two possible sources contributing to ε: (a) thermal strains, and (b) strains due to a phase change [Liang and Rogers, 1990; Bhattacharyya and Lagoudas, 1997]. The thermal strains are at least two orders of magnitude lower than the phase transformation strain, based on which ε is attributed to phase changes only. For the NiTi wire that was tested it was found that $\varepsilon = 0.05$. Therefore

$$A(0) = 1.05 \times A(1) \qquad , \qquad\qquad 3\text{-}20$$

with which, $\rho_{E,A}$ is calculated from Eq.3-17 as $8.371 \times 10^{-4} \ \Omega mm$.

The above tests were repeated with currents of $I = 0.3$ amps ($\theta = 30 \ ^0C$ at wire

center) to determine $\rho_{E,M}$ and $I = 0.9$ amps ($\theta = 87.2 \ ^0C$ at wire center) to determine

$\rho_{E,A}$. If the determined values turn out to be significantly different than before, then it would indicate the temperature dependence of $\rho_{E,M}$ and $\rho_{E,A}$. The results were $\rho_{E,M} = 9.728 \times 10^{-4}$ $\Omega.mm$ (a relative difference of 1.3 %) and $\rho_{E,A} = 8.275 \times 10^{-4}$ $\Omega.mm$ (relative difference of -1.1 %) and were considered relatively small compared with a change of 12.8 % between the two phases. To summarize, we take

$\rho_{E,M} = 9.603 \times 10^{-4}$ $\Omega.mm$	$\rho_{E,A} = 8.371 \times 10^{-4}$ $\Omega.mm$

3.5 Determination of convective coefficient, h_L

The temperature data obtained from the resistivity tests are used to determine convective coefficient h_L along the length of the wire. Theoretically consider the steady state temperature at the center of the SMA wire. The wire is 80 mm long, for which the temperature gradients in the vicinity of the wire center (x = 0) are expected to be minimal (see discussion in sec.2.4.2). Neglecting temperature gradients in the vicinity of x = 0, the steady state temperature at that location, $\theta(0, \infty)$, will follow from Eq.2-8 as

$$\rho_E(\xi)J^2 = \frac{2h_L}{r(\xi)}[\theta(0, \infty) - \theta_{amb}] \qquad 3\text{-}21$$

where $J = \dfrac{I}{A(\xi)}$ and $\theta_{amb} = \theta(0,0)$. The above equation then becomes

$$h_L = \frac{\rho_E(\xi)r(\xi)I^2}{2A^2(\xi)[\theta(0,\infty) - \theta(0,0)]} \qquad 3\text{-}22$$

The parameter h_L is computed at two different current values, I = 0.3 & 0.5 Amps at which $\xi = 1$ (martensite) and also at I = 0.9, 1.0 Amps at which $\xi = 0$ (austenite). The results are presented in Table.3-2. It is seen that the average value of h_L when the continuum point is in the martensitic state (see last column) is 21.2% lower than the average value of h_L when the continuum point is in the austenitic state. Therefore, ideally the model should account for this change in h_L during phase transformation. However we take the higher value of h_L (austenitic value) as the parameter h_L is held constant in the finite element scheme. The heat lost due to convection is modeled as a source term in Eq.2-8, which is a function of $\theta - \theta_{amb}$. Thus the difference in heat lost due to using the martensitic value of h_L at high temperatures ($\theta - \theta_{amb}$ is higher) will be much higher than the difference in heat lost due to using the austenitic value of h_L at low temperatures ($\theta - \theta_{amb}$ is lower). Hence we take the of h_L as the average value of the austenitic phase

$$h_L = 7.7 \times 10^{-5} \; J/mm^2.s.K$$

3.6 Determination of thermal conductivity (K_M and K_A)

The thermal conductivity was determined by using an experimental setup where one end of a wire was heated (prescribed temperature input) and the other end was connected

to a teflon block (see schematic in Fig.3-10). The entire experiment was conducted in a vacuum chamber. The governing equation for this problem follows from Eq.2-8 as

$$\frac{\partial}{\partial x}\left[K(\xi)\frac{\partial \theta}{\partial x}\right] = C_v(\xi)\frac{\partial \theta}{\partial t} - H\frac{\partial \xi}{\partial t} \qquad\qquad 3\text{-}23$$

where we have set $J = 0$ (no electrical heating), $h_L = 0$ (no convection). The boundary conditions were taken as

$$\theta(0,t) = \overline{\theta}(t) \qquad \text{and} \qquad \frac{\partial \theta}{\partial x}(L,t) = 0 \qquad , \qquad 3\text{-}24$$

where $\overline{\theta}(t)$ is a prescribed temperature input at the end, $x = 0$, of the wire (where the wire was connected to a resistor) and L is the wire length. The initial condition was taken as

$$\theta(x,0) = \theta_{amb} \qquad\qquad 3\text{-}25$$

In order to validate the above assumptions, the experiment was performed first with a nichrome (Ni-Cr) wire for which the thermal conductivity was known to be $K = 1.2636$ x 10^{-2} J/(mm.s.K) up to 60 ^{0}C (Omega Inc.). The basic apparatus consisted of a steel base plate and a vacuum chamber (glass bell jar sealed with vacuum grease) powered by a trivac D8A vacuum pump capable of operating up to a maximum pressure of 10^{-4} mbars (1.0×10^{-2} Pascals). The base plate shown in the diagram was attached to a leak-proof joint through which all wires are run. The joint was maintained at a uniform ambient temperature in accordance with the basic precautions for temperature measurement. All wires to and from the vacuum chamber were shielded and properly grounded to eliminate noise and interference. An in-house test jig was constructed specially for this experiment that fits into the vacuum chamber. The test jig consists of three main components. The first component includes the primary support on which the heating unit (essentially a pinned 50 ohm resistor with a soft sheath embedded in a teflon block) was mounted. The

second component consists a small pulley with 2000 grams on one side and a teflon coupling on the other side. The wire (whose thermal conductivity is to be experimentally determined) was used to connect the resistor and the teflon coupling as shown in Fig.3-10. Note that the experiment was done in vacuum, hence there was no possibility for heat loss (assuming no convection) from the test wire except due to conduction through the end connected to the teflon coupling. Teflon is a very poor conductor of heat and thus prevents heat loss by conduction. Also great care was taken while attaching the wire to the teflon piece so that the thermal mass of the joint itself is kept to a bare minimum. The third component of the test jig consisted of three pre-calibrated thermocouples (same as described in previous sections) with special holders attached to the test jig itself. The three thermocouples were attached to the test wire at three different points and temperatures were measured similar to the procedures outlined in earlier sections. The thermocouple closest to the resistor was connected in series with a control switch that acted as a trigger for the power circuits that heated the resistor. This was done for safety reasons such as overheating and failure of thermocouples.

The length of the nichrome wire was 19.6 mm and three thermocouples were positioned at x = 0, 5.3 and 11.9 mm respectively. The air in the chamber was removed using the vacuum pump until a pressure of 10^{-2} mbars (1.0 Pascals). The $\theta(x,t) - t$ measurements at the three locations are shown in Fig.3-11 and the corresponding finite element simulation was done using Eqs.3-23 & 3-24 wherein we set $K_A = K_M = 1.2636 \times 10^{-2}$ J/(mm.s.K) and $C_{V,A} = C_{V,M} = 3.8669 \times 10^{-3}$ J/mm³.K, and $H = 0$ (no phase transformation). The first thermocouple reading (marked 1 in Fig.3-11) was incorporated as a boundary condition in Eq.3-24, $\bar{\theta}(t)$, and was modeled in the finite

element code by linear interpolation of the data points during each time step. Temperature values between consecutive measurements are found by linear interpolation. The ambient temperature was taken as $\theta_{amb} = 20.85$ degC. The results of the finite element calculation are the predictions of the second and third thermocouple readings. The predictions are seen to be quite reasonable, specifically at lower temperatures.

The experiment was now repeated with a Ni-Ti wire of length, L = 15.2 mm with 2000 grams attached to one end. Three thermocouples were positioned at x = 0, 3.1 and 6.5 mm. With this weight, $A_S = 67\ ^0C$, $A_F = 72\ ^0C$ (determined from Eq.2-4a, wherein we set D = 18.49 MPa/ ^0C). Since the ambient temperature was 20.85 ^0C, the wire was expected to be in a fully martensitic condition under the given stress condition. The wire was heated at one end with the resistor and the thermocouple readings are recorded. The approach to determine K_A and K_M is now described. Note that as long as the temperature at a location is below $A_S = 67\ ^0C$, that continuum point was still in a martensitic condition. We use Eqs.3-23 to 3-25 to simulate all temperature data points for the third thermocouple with various values of K_M. Since the third thermocouple was the farthest from the boundary condition imposed, it will have the least possibility for error. Thus with a given K_M, the computed temperature profile at x = 6.5 mm was used to calculate an error quantity defined as

$$error = \frac{1}{N}\sum_{i=1}^{N}[\theta_{FEM}(x,t_i) - \theta_{EXP}(x,t_i)]^2 \qquad\qquad 3\text{-}26$$

where t_i is the ith value of time and N is the total number of data points below $A_S = 67\ ^0C$. The error calculated has been plotted in Fig.3-12 as a function of K_M. The

lowest value of error corresponds to $K_M = 1.4 \times 10^{-2}$ J/(mm.s.K). With K_M now

determined, Eqs.3-23 to 3-25 are used again to simulate the temperature at x = 6.5 mm

(third thermocouple) beyond $A_F = 72\ ^0C$. Various values of K_A are used to calculate the

error as shown in Fig.3-13. The lowest error corresponds to

$K_A = 2.8 \times 10^{-2}$ J/(mm.s.K). With these values of K_M and K_A, the second thermocouple

reading at x = 3.1 mm is predicted and the comparison is seen to be reasonable as shown

in Fig.3-14. The effect of a variable thermal conductivity is quite significant as evident in

Fig.3-15 wherein we have set $K_A = K_M$ and taken this value to be of martensite. The

significant discrepancies at higher temperatures are obvious. A complete list of all

properties is given in Table.3-3. In summary

$$K_M = 1.4 \times 10^{-2}\ J/(mm.s.K)\quad , \qquad K_A = 2.8 \times 10^{-2}\ J/(mm.s.K)$$

3.7   The displacement – temperature - time characteristics of Ni-Ti wire actuator

Finally as part of the characterization of thermally induced phase transformations,

we study the displacement - temperature - time characteristics of the given Ni-Ti thin

wire. The material properties measured in the previous chapter (as listed in Table 3-3) are

used along with the finite element code (discussed in Chap.2) to simulate the temperature

- time characteristics and the strain - time characteristics, which are then compared with the experimentally observed data.

The setup was similar to that of previous experiments as described in the preceding sections, with some modifications. A schematic representation of the apparatus and setup used is given in Fig.3-16. The apparatus consisted of a Ni-Ti (0.381 mm dia) wire of length 80 mm, pinned to Teflon ends and subjected to a constant load of 19.62 N. A thermocouple (0.0254 mm dia Type J Iron-Constantan) was attached to the center of the wire and connected to a Hewlett Packard − 7101B strip chart recorder to monitor temperature. A Durham Instruments Inc., (type 500 dc-e) Linear Voltage Displacement Transducer was used in series with the Ni-Ti wire and connected to a HP 7044a plotter to monitor the transformation strain with a total displacement range of ± 25.4 mm. The entire apparatus was covered with a glass and metal box to prevent local air currents and external noise from influencing the measurements. Detailed calibration procedures for the various equipment used for measuring temperature and strain in this experiment is given in Appendix B. The wire was heated for 30 sec, during which time the $M \rightarrow A$ transformation takes place. The power is then switched off allowing the wire to cool ($A \rightarrow M$ transformation). Several trials were conducted where the temperature - time response and the displacement - temperature relationship was obtained for different current densities. Fig.3-17 gives the temperature - time response of the Ni-Ti thin wire measured at its center under a constant current of 0.9 Amperes. Also included in the figure are two solid lines corresponding to FEM simulation of 'constant properties' and 'variable properties' for the Ni-Ti wire as listed in Table.3-3. For the 'constant properties' case, we take the properties of martensite as it is the initial phase during

simulation. The start and finish temperatures, M_S and M_F, during cooling are taken as 41 ^0C and 46 ^0C respectively (Dynalloy Inc.). Clearly, the 'variable properties case simulates the experimental data better than the 'constant properties' case. Note that the transformation time is significantly different between the two simulated cases confirming the conclusions arrived with the parametric studies given in Sec.2.5.

Fig.3-18 shows the overall strain of the SMA wire with respect to time; the experimental curve is given along with the FEM simulation ('constant properties' and 'variable properties'). In the FEM simulation, the strain, $\bar{\varepsilon}$, is taken proportional to the overall martensite volume fraction, $\bar{\xi}$, given as [Bhattacharyya A, Amalraj J and Faulkner M G, 1999]

$$\bar{\varepsilon} = \bar{\varepsilon}_{total} \times \bar{\xi} \qquad , \qquad 3\text{-}27$$

where $\bar{\varepsilon}_{total}$ is the total strain when $\bar{\xi} = 1$ (martensite phase), measured as 5%. We see that the influence of variable properties makes the simulation curves tend much closer to the experimental results. The strain – time relationship shows considerable difference at the start and at the end of transformation. This can be attributed to the effect of localized stress concentrations typical of polycrystals. i.e although the overall stress applied on the wire is uniform, the local stresses in a ploycrystal wire can be higher or lower than the applied stress at certain areas thereby making the wire transform either before or after the expected transformation range (comparison of DSC curve in Fig.3-6). This is to be expected since the wire is quite 'long' which allows for more imperfection and impurities. However, the effect of the electrical resistivity can be clearly seen as the total cycle time of the simulation as well as the rate of transformation is much better in the variable properties case.

In summary, the comparison of the temperature – strain relationship, and strain – time relationship clearly shows that variable properties affect the phase transformation and the evolution of the material properties cannot be ignored. The experimental work described in this chapter also reaffirms the conclusions arrived at in Chapter 2. The research also shows that there can be improvements to modeling the martensitic volume fraction.

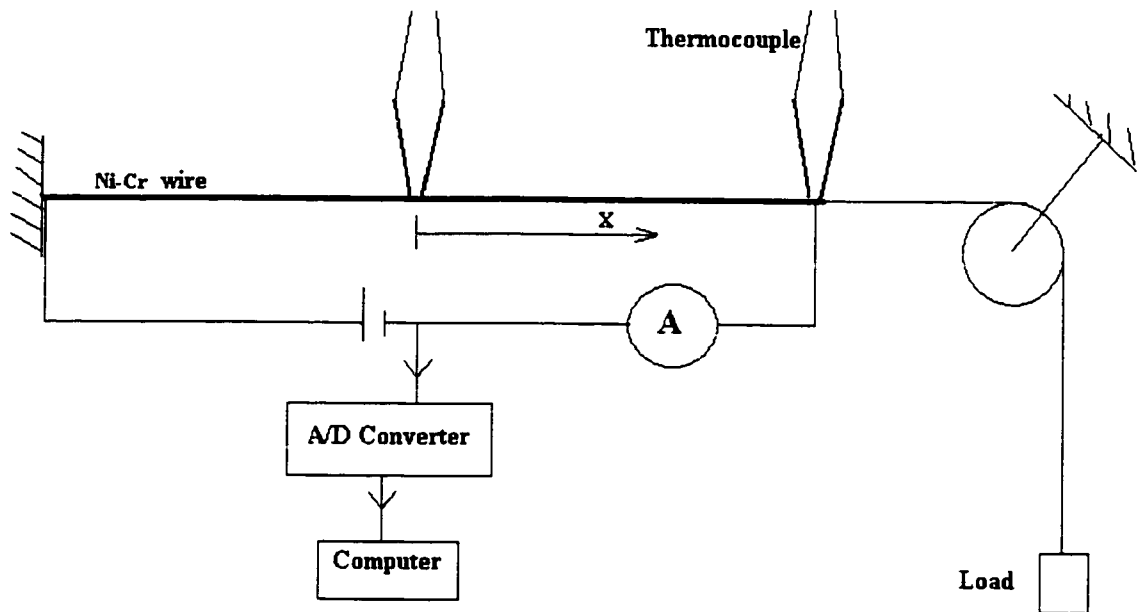Figure.3-1 Schematic showing the experimental setup for the validation of the boundary

conditions.

Figure.3-2 Comparison of the theoretical and experimental temperature profiles at the

center of the Ni-Cr wire.

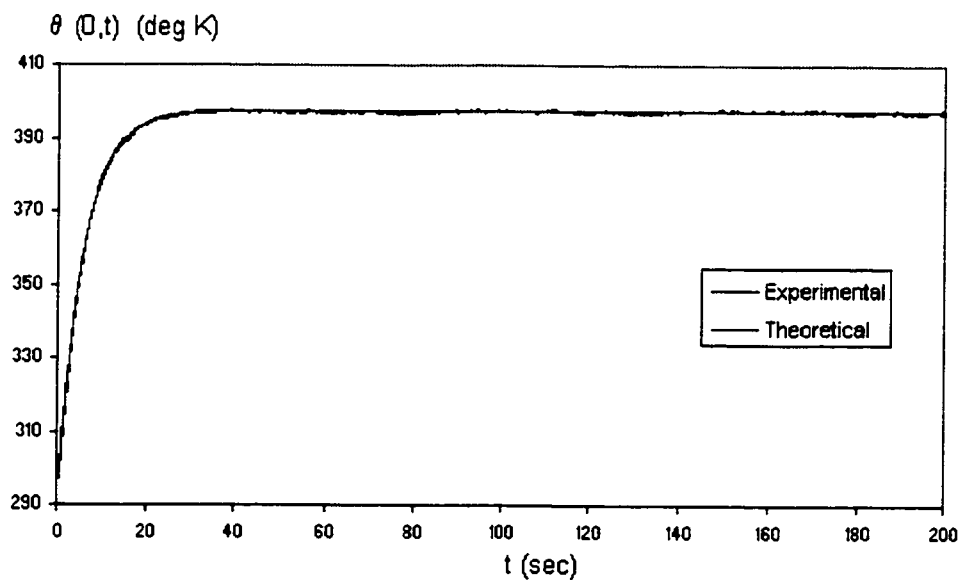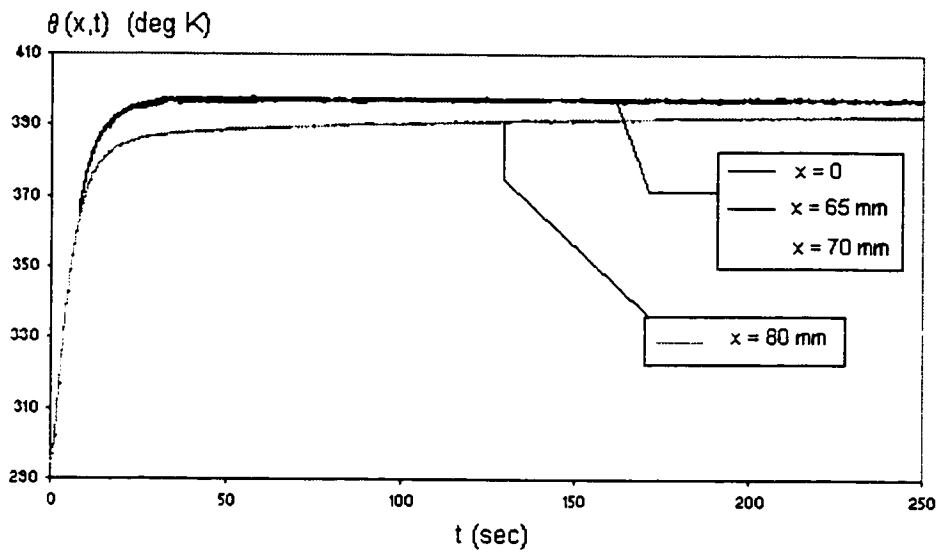Figure.3-3 Plot showing experimentally observed temperature profile at various points of

the Ni-Cr wire.
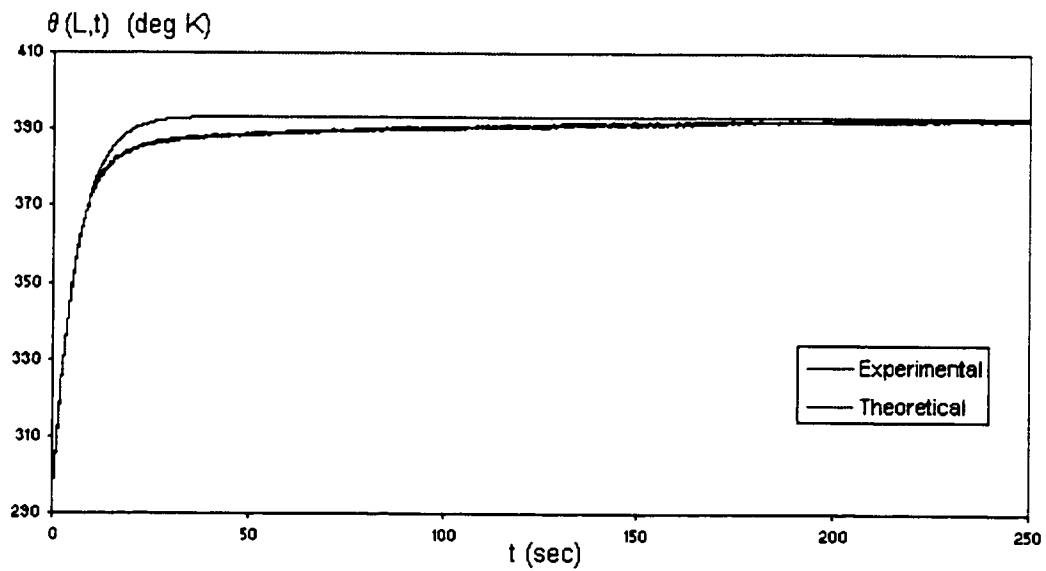
Figure.3-4 Comparison of the theoretical and experimental temperature profiles at the

end of the Ni-Cr wire.

DSC
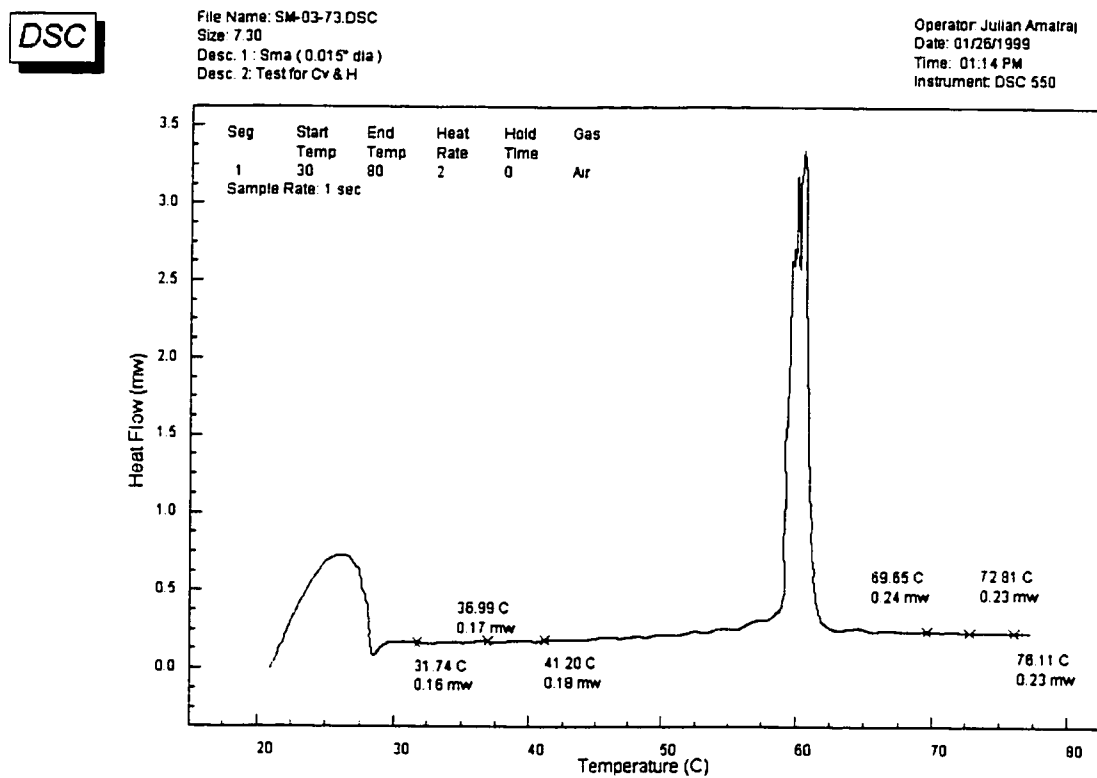
Figure.3-5 DSC thermogram showing various stages of phase transformation in Ni-Ti

thin wire specimen.

$\dot{Q}/(\dot{\theta}V)$ (J/mm^{3}K)
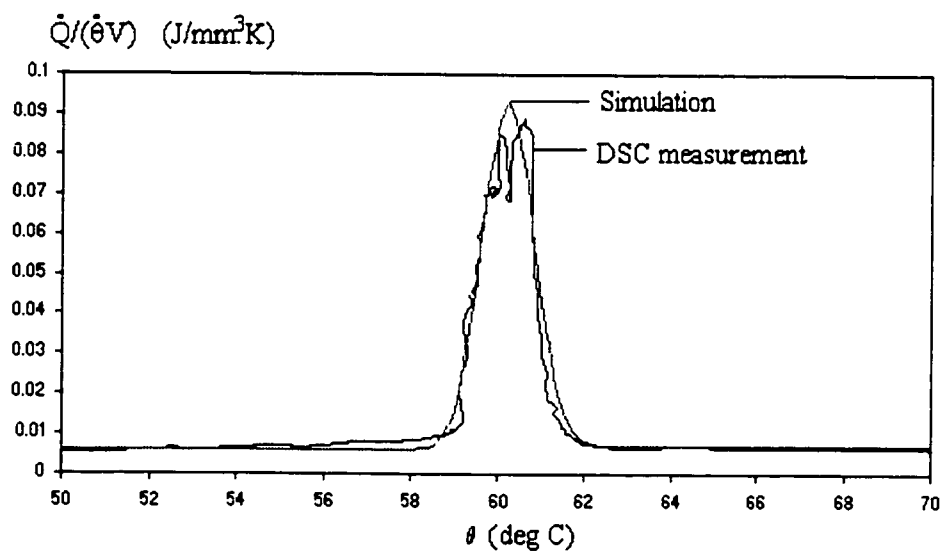
Figure.3-6 Simulation of DSC curve for a SMA sample.
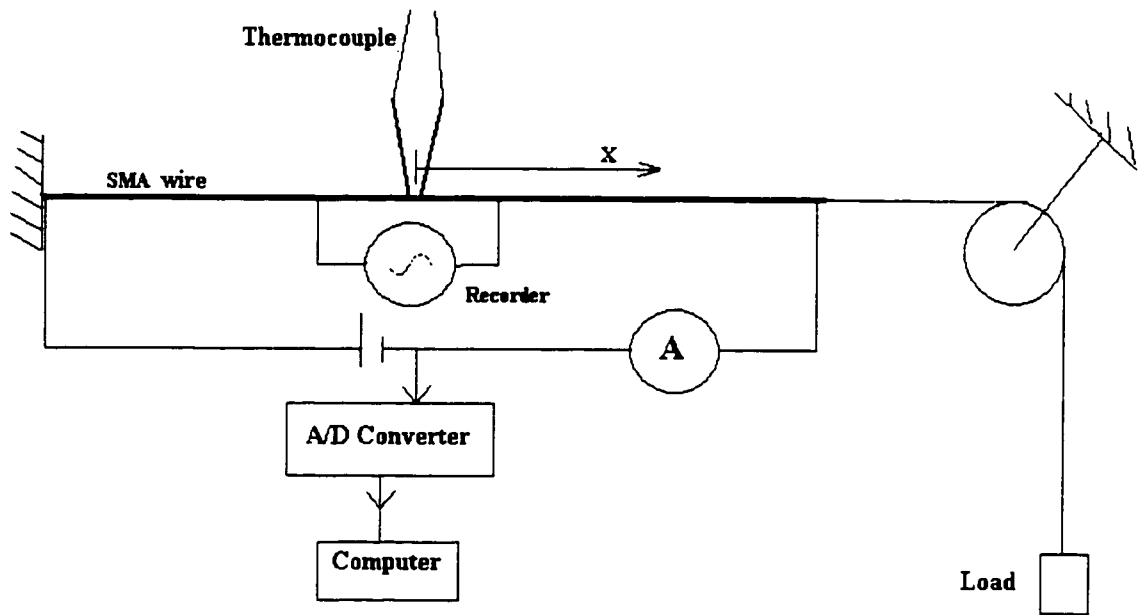
Figure.3-7 Schematic representation of the experimental setup for measurement of

electrical resistivity.

R (L_2,0) (ohms)
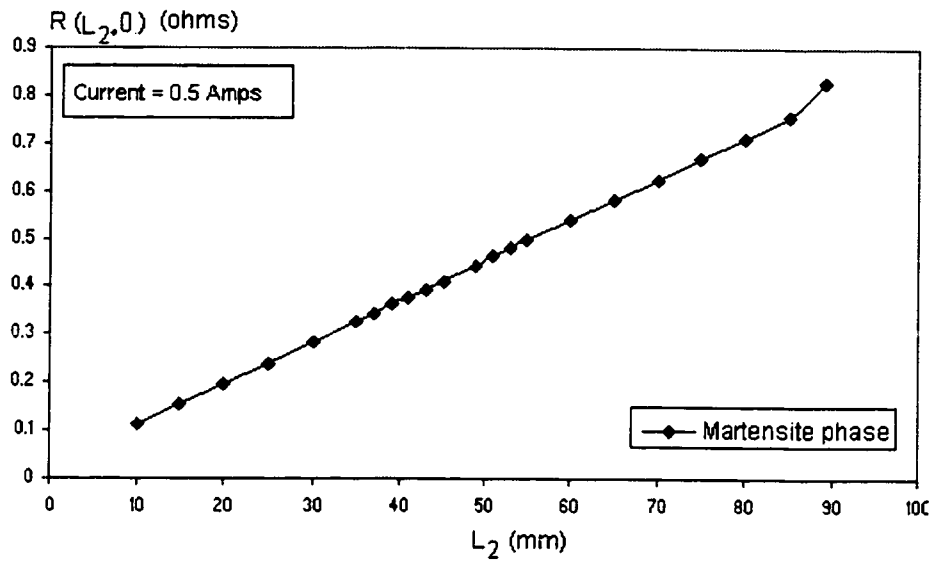
Figure.3-8 Plot showing resistance with length of test section for the martensitic phase of

Ni-Ti wire.

R (L_2,0)(ohms)
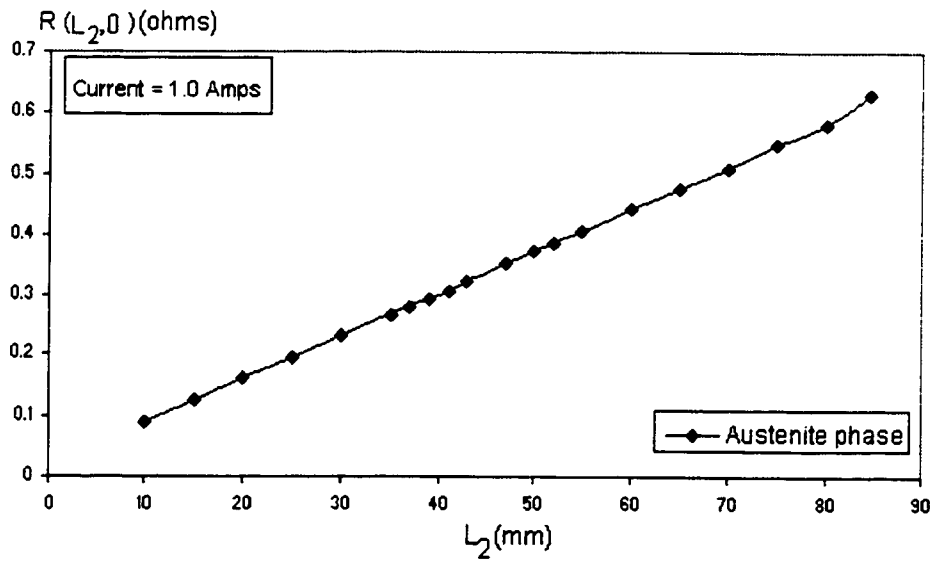
Figure.3-9 Plot showing resistance with length of test section for the austenitic phase of

Ni-Ti wire.
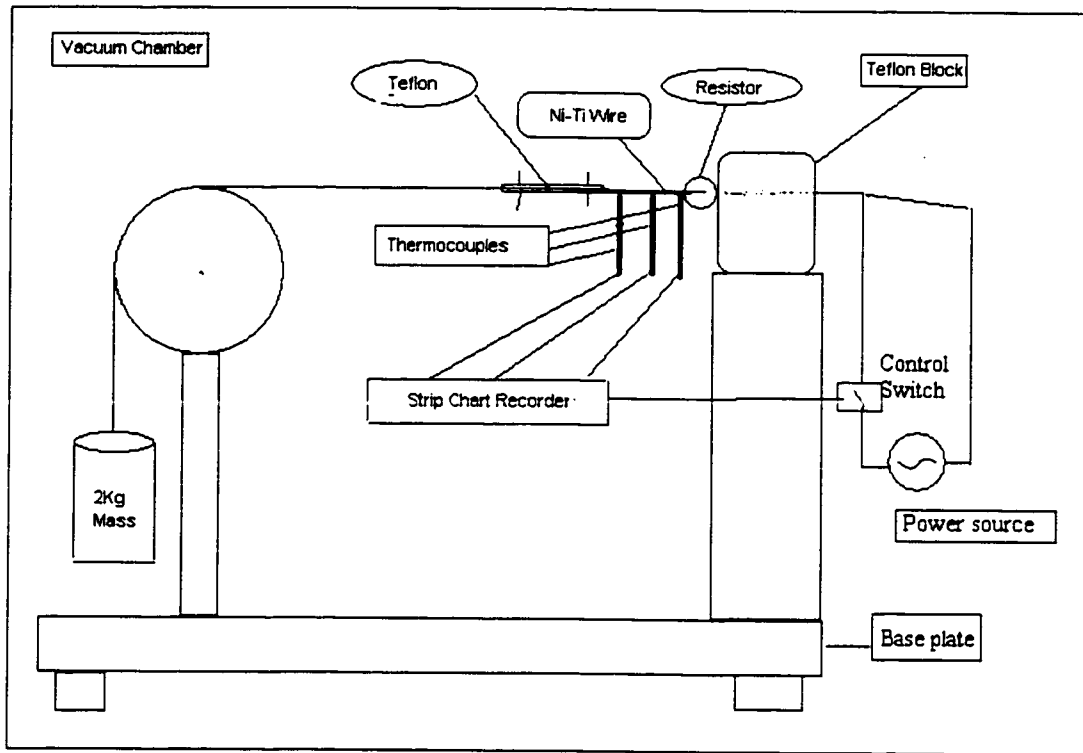
Figure.3-10 Schematic representation of the experimental setup for measuring thermal

conductivity of Ni-Ti wire.
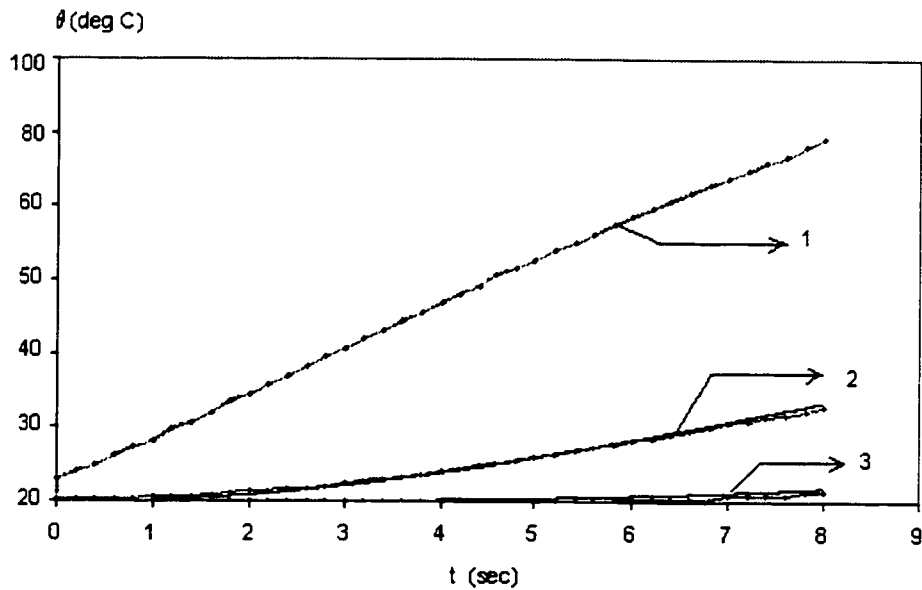
Figure.3-11 Plot showing comparison of experimental and simulated temperature

profiles for Ni-Cr wire with thermal conductivity k = 1.2636 x 10^{-2} J/(mm.s.K).

Figure.3-12 Plot showing error in temperature due to thermal conductivity for martensite

phase.
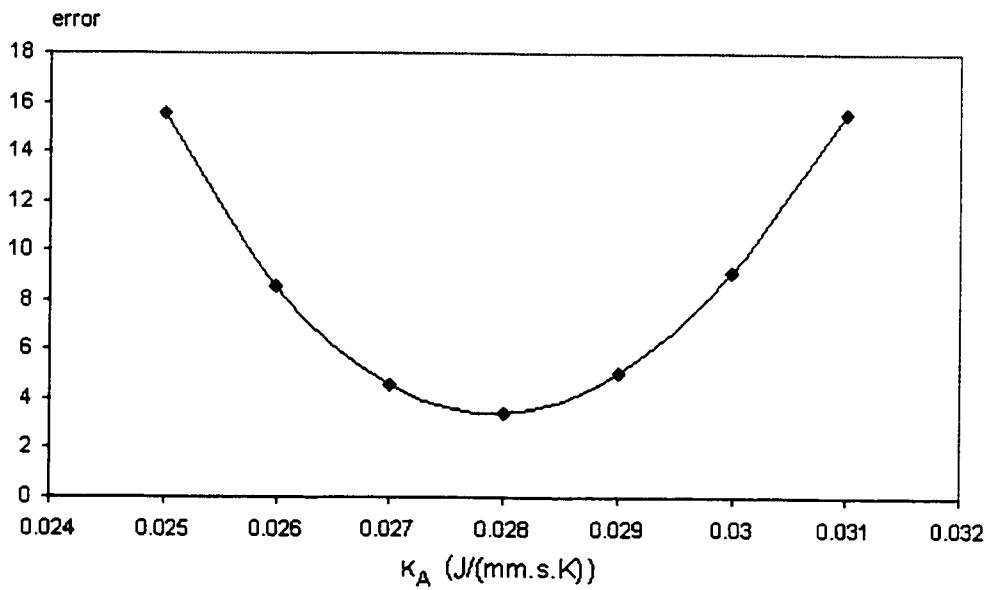
Figure.3-13 Plot showing error in temperature due to thermal conductivity for austenite

phase.
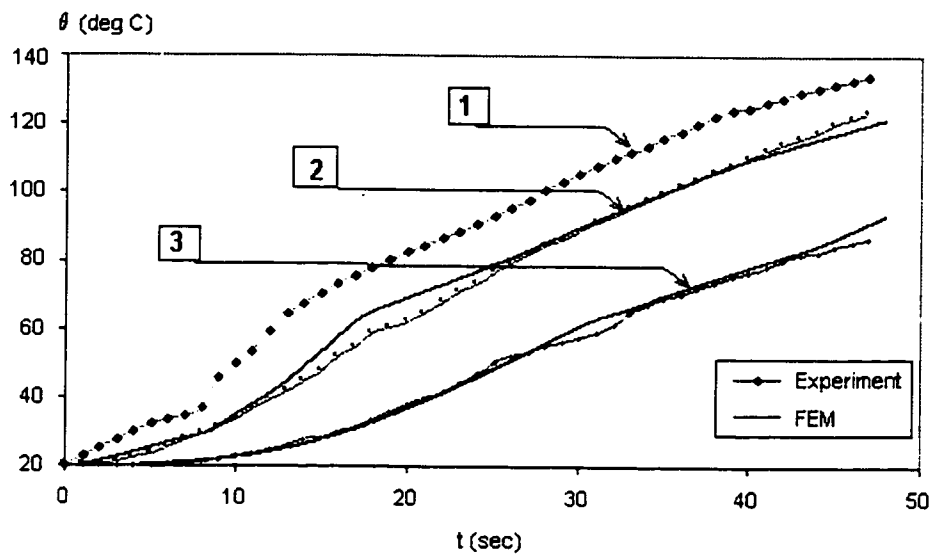
Figure.3-14 Plot showing comparison of experimental and simulated temperature values

for best fit thermal conductivity in both phases.
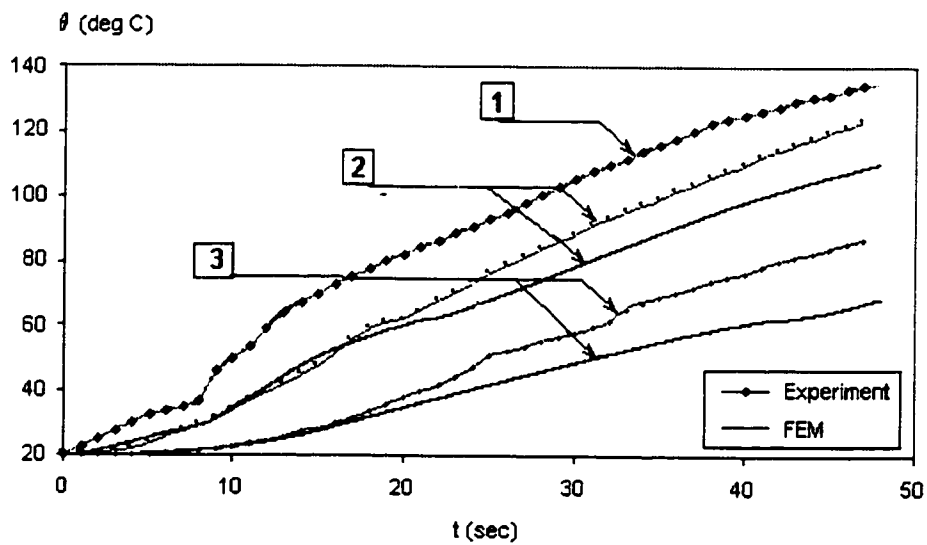
Figure.3-15 Plot showing comparison of experimental and simulated temperature values

for best fit thermal conductivity in the martensite phase.
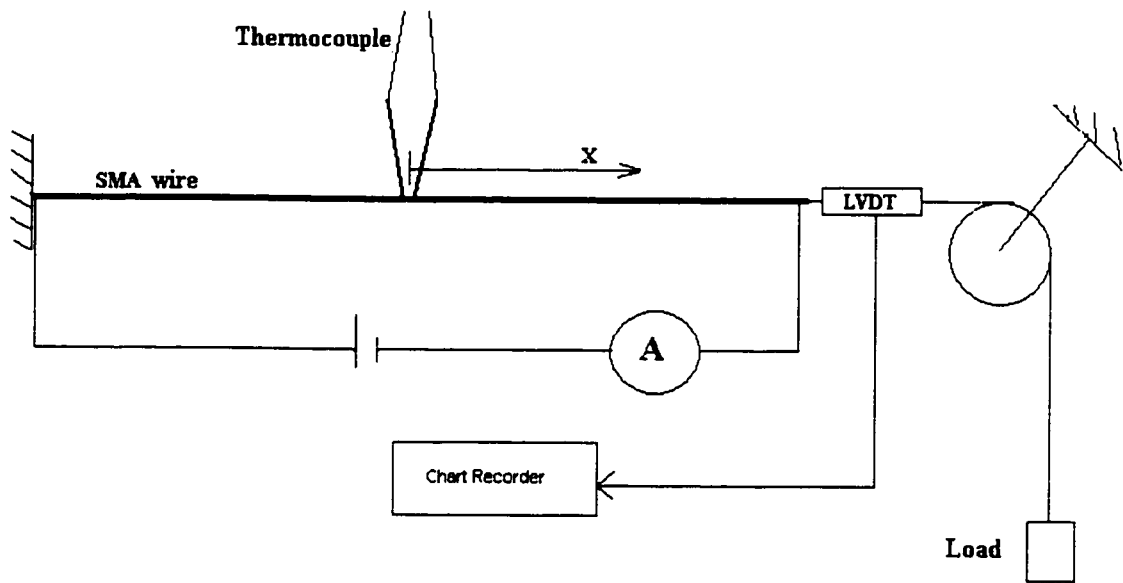
Figure.3-16 Schematic diagram of the experimental setup for the thermo-mechanical

characterization of given Ni -Ti thin wire.
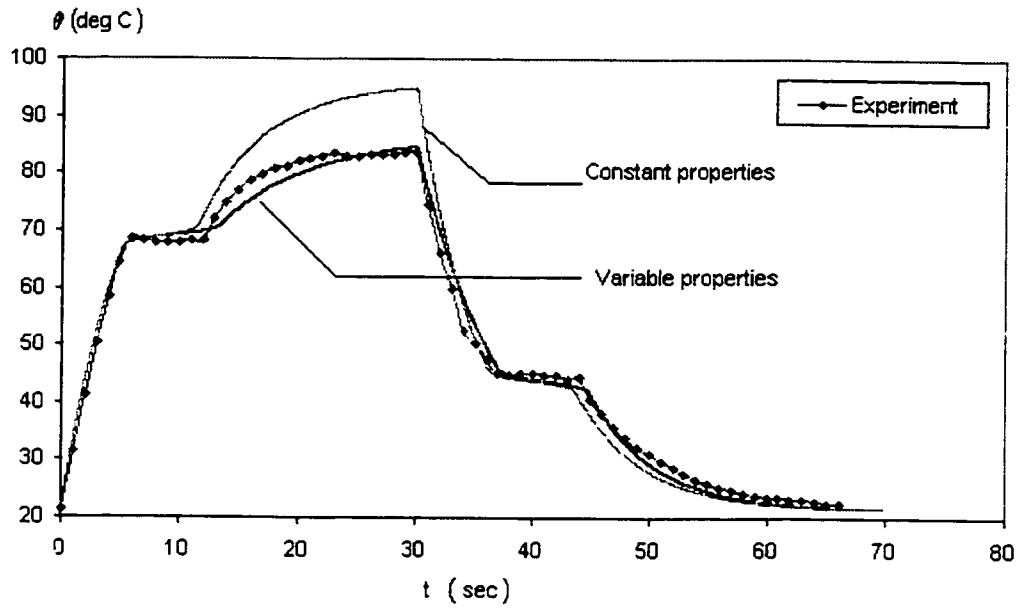
Figure.3-17 Comparison of Experimental temperature - time response with the

corresponding FEM simulation.
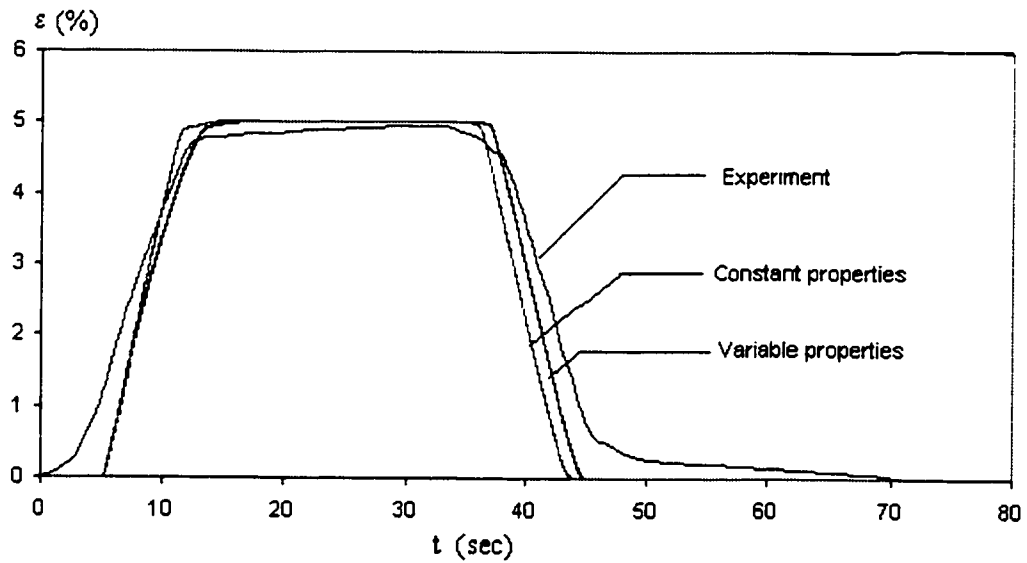
Figure.3-18 Plot showing comparison of experimentally observed strain with that of

FEM simulation for given Ni-Ti wire.

Property (Symbol)	Manufacturer Values (obtained from Omega. Inc)
Thermal Conductivity (K)	1.2636×10^{-2} J/(mm.s.K)
Heat Capacity (C_V)	3.689×10^{-3} J/(mm^3.K)
Electrical resistivity (ρ_E)	1.893×10^{-3} Ω.mm

Table.3-1 Values for nichrome material parameters.

I (Amps)	ξ	$R(\xi)$ (mm)	$\rho_E(\xi)$ $10^{-4}(\Omega.mm)$	$A(\xi)$ (mm^2)	$\theta(0,\infty)$ (C)	$\theta(0,0)$ (C)	h_L $10^{-5}(J/mm^2.s.K)$	Average h_L $10^{-5}(J/mm^2.s.K)$
0.3	1	0.1905	9.731	0.1140	30.2	19.58	6.0	6.07
0.5	1	0.1905	9.603	0.1140	48.2	19.58	6.15	
0.9	0	0.1952	8.278	0.1197	83.2	22.48	7.52	7.7
1.0	0	0.1952	8.37	0.1197	92.9	20.55	7.88	

Table.3-2   Tabulated values of experimental convective coefficient to the corresponding temperature and phase.

Property (Symbol)	Experimental Value
Thermal Conductivity (K_M)	1.4×10^{-2} J/(mm.s.K)
Thermal Conductivity (K_A)	2.8×10^{-2} J/(mm.s.K)
Heat Capacity ($C_{V,M}$)	4.506×10^{-3} J/(mm^3.K)
Heat Capacity ($C_{V,A}$)	5.92×10^{-3} J/(mm^3.K)
Electrical resistivity ($\rho_{E.M}$)	9.603×10^{-4} Ω.mm
Electrical resistivity ($\rho_{E.A}$)	8.371×10^{-4} Ω.mm
Latent heat (H)	0.125 J/mm^3
Convective coefficient (h_L)	7.7×10^{-5} J/(mm^2.s.K)
A_S, A_F	57.5, 62.5 deg C
Radius of the wire (r)	1.905×10^{-01} mm

Table.3-3 Summary of material properties measured experimentally for the given Ni-Ti wire.

4. CONCLUSIONS AND FUTURE WORK

4.1 Conclusions

The main aim of this research was to investigate the effect of varying material properties on purely thermal phase transformations in SMA polycrystal wire actuators. Based on our literature survey (refer Sec1.2) it was clear that while there was considerable work done towards constitutive modeling of SMA behavior, almost all researchers have overlooked the evolution of material properties and their effect on the phase transformation itself. This can lead to reduced effectiveness of design and control models that are used in simulating SMA behavior, thus contributing to improper implementation of these actuators into smart structures. Hence there was a need to study the evolution of relevant material properties and their effect on the phase transformation. Also the lack of data on the material properties in literature can be attributed to the lack of properly documented experimental procedures that help measure accurately the change in properties while taking into account the unique nature of the SMA alloys. This is precisely what we dealt with in this thesis.

The major conclusions drawn from the parametric studies done with the developed FEM scheme in the first phase of research are:

1. Varying material properties has a considerable effect on the phase transformations and the variations cannot be ignored for proper modeling and control of the SMA actuator.

2. Electrical resistivity directly affects the frequency of actuation (rate at which the phase transformation proceeds). An increase in electrical resistivity during phase transformation results in a decrease in the phase transformation time and vice-versa.

3. Thermal conductivity affects the average martensitic volume fraction (thereby affecting the amount of wire transformed). If the actuator wire has a half-length that can be considered 'long' (>50 mm for a 0.127 mm dia wire) then the thermal behavior of the wire tends closer to the adiabatic case. An increase in thermal conductivity during phase transformation also results in the wire exhibiting a behavior closer to the adiabatic case even though the wire is subjected to the isothermal boundary condition.

4. In case of very short wire actuators (<10 mm for a 0.127 mm dia wire) as in the case of micro-actuators, thermal conductivity affects the frequency of phase transformation and the average martensitic volume fraction.

5. The effect of heat capacity as such on the thermal behavior of the SMA actuator can be considered small.

6. The combined effect of both varying electrical resistivity and thermal conductivity is relatively small compared to their effect individually, but can be expected to have a considerable effect when cyclic effects are the issue.

The second component of the research involved developing experimental procedures that can effectively measure the property variations as a function of the new phase generated while taking into account the unique nature of the SMA phase transformation when measuring the properties. The developed techniques were then used to measure property variations of a equi-atomic Ni-Ti wire and the major results are as follows :

1. The end grips of the wires were modeled as a convective boundary and the equivalent convective coefficient was found to be $h_B = 4.5 \times 10^{-4}$ J/mm^2.s.K.

2. The experiments showed that there was a variation of 12.8 % in electrical resistivity, 31.3 % change in heat capacity and a 100% change in thermal conductivity between the two phases of austenite and martensite.

3. The convective coefficient along the length of the wire was found to be $h_L = 7.7 \times 10^{-5}$ J/mm^2.s.K. Although there were considerable variations in the values of h_L, the value of austenitic phase was used for better accuracy (see Sec3.5 for details).

4. The temperature – time simulation using the measured material properties for both phases obtained experimentally agreed very well with the observed experimental behavior and were better than the assumption of constant properties.

5. The results also confirmed the conclusions observed in the parametric studies, thus proving that variations in material properties must be accounted for while modeling SMA transformations.

6. There were considerable deviations in strain at the start and the end of phase transformation that can be attributed to local stress concentrations, which need to be addressed to improve the constitutive modeling itself.

7. The developed techniques were not material specific and hence can be used to measure variations in material properties for other alloys.

4.2 Future work

The two major components of the research have been concerned with SMA wires. The finite element scheme can be further improved by considering the thermo-elastic relationship during phase transformation. This will improve the modeling of strain – time relationship and the temperature – strain relationship of the given SMA wire. The FEM scheme can also be further extended to include modeling of thin films (2-D) and SMA rods (3-D), which when done will prove to be a very useful tool in the design and implementation of SMA alloys in various configurations in smart structures. Since the finite element scheme is a generalized approach, various functions that describe the evolution of material properties can be developed and tested to accurately describe the corresponding property evolution. This is crucial as the finite element scheme can be used effectively to study the evolution of various material parameters that affect phase transformation over a number of cycles (cyclic behavior of the various properties and their effect on the overall response of the SMA wire).

The second component of the research resulted in robust experimental procedures that can accurately measure the variations in material properties for each phase of the SMA alloy. While our research concentrated on measuring the property values for equi-atomic Ni-Ti wire, the above-mentioned procedures can also be used to accurately measure and study the material property variations with different compositions and configurations. Such work will result in a comprehensive database on various material properties for different alloys and alloy compositions, thus giving valuable data on these alloys for modeling purposes. The work can also be extended to include stress - induced

transformations, elastic properties and their role in phase transformations. Lastly the experimental procedures discussed can be easily adapted to study other important issues in characterizing SMA polycrystal actuators like inclusions, material imperfections, cyclic behavior, fatigue and plastic deformations. The data thus obtained can be used to obtain better constitutive models that describe the SMA behavior more accurately.

BIBLIOGRAPHY

Abeyaratne R and Knowles J K 1993 A continuum model of a thermoelastic solid capable of undergoing phase transition *J. Mech . Phys. Solids* **41** 541 - 571

Abeyaratne R, Kim S and Knowles J K 1994 A one dimensional continuum model for the shape memory alloys *Int. J. Solids Structures* **25** 3273 – 3289

Benzaoui H, Lexcellent C, Chaillet N, Lang B and Bourjault A 1997 Experimental study and modeling of TiNi shape memory alloy wire actuator *J . Intelligent Material Systems & structures* **6**

Bhattacharyya K and Kohn R V 1995 Symmetry, texture and recoverable strain of shape-memory alloy polycrystals *Acta Metall. Mater.* **44** No 2 529-542

Bhattacharyya A, Amalraj J and Faulkner M G 1998 Finite element modeling of phase transformations in thin SMA wires with variable material properties (submitted)

Bhattacharyya A and Lagoudas D C 1997 A stochastic thermodynamic model for the gradual thermal transformation of SMA polycrystals *Smart Mater. Struc.* **6** 235 - 250

Bhattacharyya A, Lagoudas D C, Wang A and Kinra V K 1995 On the role of thermoelectric heat transfer in the design of SMA actuators: Theoretical modeling and experiment *Smart Mater. Struc* **4** 252

Bo Z, Kurdila A J, Lagoudas D C and Webb G Identification for a class of nonlinear models for SMA embedded elastomeric rods, in *Active Materials and Structures. Proceedings of the 31st annual meeting of the Society of Engineering Sciences, College Station, Texas,* Vol.2427, 93

Boley B A and Weiner J H Theory of thermal stresses (Krieger, Fl,1960)

Boyd J G and Lagoudas D C 1996a A thermodynamical constitutive model for shape memory materials Part I : The Monlithic shape memory alloy *Int. J. Plasticity* **12** 805-842

Boyd J G and Lagoudas D C 1996b A thermodynamical constitutive model for shape memory materials Part II : The SMA composite material *Int. J. Plasticity* **12** 843 - 873

Brinson L C 1993 One dimensional constitutive behavior of shape memory alloys: Thermodynamical derivation with non-constant material functions *Journal of Intelligent Material Systems and Structures* **4** No 2 229-242

Carslaw H and Jaeger S Conduction of heat in solids 2nd Ed. (Oxford University Press, U.K, 1959)

Duerig T W, Melton K N, Stockel D and Wayman C M 1990 Engineering aspects of shape memory alloys (Butterworth-Heinemann, London)

Dynalloy, Inc. *Instruction for the FLEXINOL^{TM} Sample Kit* Irvine, CA, USA

Escobar J C, and Clifton R J 1994 Pressure shear impact induced phase transformations in Cu-14.44 Al-4.19Ni single crystals in *Active Materials and Structures, Proceedings of the 31st annual meeting of the Society of Engineering Sciences, College Station, Texas,* Vol.2427, 186

Funakabo H 1984 Shape memory alloys (New York: Gordon and Breach Science publishers)

Giurgiutiu V, Chaudry Z and Rogers C 1995 Energy-based comparison of solid-state actuators (Technical report) *Centre for intelligent Material Systems and Structures* VPI-SU, Blacksburg, VA

Jackson C M, Wagner H J and Wasilewski R J 1972 The alloy with a memory: Its physical metallurgy, properties and applications *NASA-SP 5110*

Krulevitch P, Lee A P, Ramsey P B, Trevino J and Northrup M A 1996 Thin film shape memory alloy microactuators *Micro Electro Mechanical Systems (MEMS) American Society of Mechanical Engineers, Dynamic Systems and Control Division (Publication) DSC.* **59**, *ASME,* New York, NY, USA 301-306

Lagoudas D C and Bhattacharyya A 1998 Modeling of thin layer extensional thermoelectric SMA actuators *Int. J. Solids Structures* **35** 331-362

Lagoudas D C, Bo Z and Bhattacharyya A 1996 A thermodynamic constitutive model for gradual phase transformation of SMA materials *Proceedings of the SPIE Conference,* San Diego, CA

Lagoudas D C, Moorthy D, Qidwai M A and Reddy J N 1997 Modeling of the thermomechanical response of active laminates with SMA strips using the layerwise finite element method *Journal of Intelligent Material Systems and Structures* **8** No 6 476 - 488

Leo P H, Shield T W and Bruno O P 1993 Transient heat transfer effects on the pseudoelastic behavior of shape memory wires *Acta Metall. Mater* **41** 2477 - 2485

Liang C and Rogers C A 1990 One dimensional thermomechanical constitutive relations of shape memory materials *Journal of Intelligent Material Systems and Structures* **1** 207 - 234

Liang C and Rogers C A 1997 Design of shape memory alloy springs with applications in vibration control *Journal of Intelligent Material Systems and Structures* **8** No 4 314 - 322

Miyazaki S, Otsuka K and Suzuki Y 1981 Transformation pseudoelasticity and deformation behavior in a Ti-50.6 at % Ni alloy *Scripta. Metall.* **15** 287 - 292

Oberaigner F R, Tanaka K and Fischer F D 1996 Investigation of the damping behavior of a vibrating shape memory alloy rod using a micromechanical model *Smart Mater. Struct.* **3** 456 -463

Patoor E, Eberhardt A and Berveiller M 1987 Potential pseudoelastique et plasticite de transformation martenistique dans les mono-et polycristaux metallique. *Acta Metallurgica* **35**, 2779

Perkins S J and Sponholz R 1984 Stress induced martensitic transformation. cycling and two-way shape memory training in Cu-Zn-Al alloys *Metallurgical Transactions* **15A**, 313

Raniecki B and Lexcellent C 1994 R$_L$ models of pseudoelasticity and their specification for some shape memory solids *Eur . J. Mech* **13A**, 21

Sato Y and Tanaka K 1988 Estimation of energy dissipation in alloys due to stress induced martensitic transformation *Res Mechanica* **23**, 381

Shaw J and Kryiakides S 1995 On the themomechanical behavior of NiTi *Journal of Mechanics and Physics of Solids* **43** 1243 - 1282

Shu G S, Lagoudas D C, Hughes D and John W T 1997 Modeling of a flexible beam actuated by shape memory alloy wires *Smart Mater. Struct.* **6** 265 - 277

Tanaka K, Tsukamoto H and Tanaka H 1995 Improvement of span-wise deflecting flow by shape-controlled airfoils *Fluid Machinery American Society of Mechanical Engineers, Fluids Engineering Division (Publication) FED* **222** ASME, New York, NY, USA 123 - 127

Thompson D M and Griffin O H Jr 1993 Finite element predictions of active buckling control of stiffened panels *Journal of Intelligent Material Systems and Structures* **4** No 2 243 - 247

Wei Z G, Tang C Y and Lee W B 1997 Design and fabrication of intelligent composites based on shape memory alloys *Journal of Materials Processing Technology* **69** No 1-3 68 - 74

APPENDIX A

1. Components of A^* and $\bar{B}^*$

The non-zero matrix elements of the matrix A^*, and elements of vector $\bar{B}^*$ (see Eq.2-29) are now given. As a first step, components of a matrix $A^{*,\,UN}$ and vector $\bar{B}^{*,UN}$ are given, using which, we then give components of A^* and $\bar{B}^*$.

$$A^{*,UN}_{q\,q} = \frac{K\left(\bar{\xi}^q_*\right)}{\Delta L_q} + \frac{2h_L \Delta L_q}{3r} + \left[C_V\left(\bar{\xi}^q_*\right) - H\left(\frac{\partial \xi}{\partial \theta}\right)^q_*\right]\frac{\Delta L_q}{3\tau} \qquad , \quad q = 1 \text{ and } N. \qquad \text{A.1}$$

$$A^{*,UN}_{q\,q+1} = A^{*,UN}_{q+1\,q} = \frac{2h_L \Delta L_q}{6r} - \frac{K\left(\bar{\xi}^q_*\right)}{\Delta L_q} + \left[C_V\left(\bar{\xi}^q_*\right) - H\left(\frac{\partial \xi}{\partial \theta}\right)^q_*\right]\frac{\Delta L_q}{6\tau} \quad , \quad 1 \le q \le N-1 \qquad \text{A.2}$$

$$A^{*,UN}_{q\,q} = \frac{K\left(\bar{\xi}^q_*\right)}{\Delta L_q} + \frac{2h_L \Delta L_q}{3r} + \left[C_V\left(\bar{\xi}^q_*\right) - H\left(\frac{\partial \xi}{\partial \theta}\right)^q_*\right]\frac{\Delta L_q}{3\tau}$$

$$+ \frac{K\left(\bar{\xi}^{q-1}_*\right)}{\Delta L_{q-1}} + \frac{2h_L \Delta L_{q-1}}{3r} + \left[C_V\left(\bar{\xi}^{q-1}_*\right) - H\left(\frac{\partial \xi}{\partial \theta}\right)^{q-1}_*\right]\frac{\Delta L_{q-1}}{3\tau} \qquad , \quad 2 \le q \le N-1 \quad .$$

<div align="right">A.3</div>

$$B^{*,UN}_q = \frac{\rho_E\left(\bar{\xi}^q_*\right)J^2 \Delta L_q}{2} + \left(K_M - K_A\right)\left(\frac{\partial \xi}{\partial \theta}\right)^q_* \frac{\left(\theta^{q+1}_* - \theta^q_*\right)^2}{\Delta L_q}$$

$$+ \left[C_V\left(\bar{\xi}^q_*\right) - H\left(\frac{\partial \xi}{\partial \theta}\right)^q_*\right]\Delta L_q \left(\frac{\theta^{q+1}_i}{6\tau} + \frac{\theta^q_i}{3\tau}\right) \qquad \qquad \text{A.4}$$

$$+ h_L \theta_{amb} \Delta L_q \qquad \qquad , \qquad q = 1 \text{ and } N$$

and

$$B_q^{*,UN} = \frac{\rho_E\left(\overline{\xi}_*^{q-1}\right)J^2\Delta L_{q-1}}{2} + \frac{\rho_E\left(\overline{\xi}_*^{q}\right)J^2\Delta L_q}{2} + \left(K_M - K_A\right)\left(\frac{\partial\xi}{\partial\theta}\right)_*^{q-1}\frac{\left(\theta_*^q - \theta_*^{q-1}\right)^2}{\Delta L_{q-1}}$$

$$+ \left(K_M - K_A\right)\left(\frac{\partial\xi}{\partial\theta}\right)_*^{q}\frac{\left(\theta_*^{q+1} - \theta_*^q\right)^2}{\Delta L_q} + \left[C_V\left(\overline{\xi}_*^{q-1}\right) - H\left(\frac{\partial\xi}{\partial\theta}\right)_*^{q-1}\right]\Delta L_{q-1}\left(\frac{\theta_i^{q-1}}{6\tau} + \frac{\theta_i^q}{3\tau}\right)$$

$$+ \left[C_V\left(\overline{\xi}_*^{q}\right) - H\left(\frac{\partial\xi}{\partial\theta}\right)_*^{q}\right]\Delta L_q\left(\frac{\theta_i^{q+1}}{6\tau} + \frac{\theta_i^q}{3\tau}\right)$$

$$+ h_L\theta_{amb}\left(\Delta L_{q-1} + \Delta L_q\right) \quad , \qquad\qquad 2 \le q \le N-1 \qquad\qquad .$$

<div align="right">A. 5</div>

All the components of $\mathbf{A}^*$ and $\overline{\mathbf{B}}^*$ are taken identical to the corresponding components of $\mathbf{A}^{*,UN}$ and $\overline{\mathbf{B}}^{*,UN}$ above except those mentioned below.

Isothermal boundary condition

This condition (Eq.2-14) is implemented based on Allaire's method of prescribed constraints[Allaire, 1984] as

$$B_N^* = \theta_{amb}A_{NN}^{*,UN} \quad ,$$

and

$$A_{Nq}^* = 0 \quad , \qquad 1 \le q \le N-1 \quad .$$

<div align="right">A. 6</div>

Convective boundary condition

When the convective boundary condition (Eq.2-13) is used, we have

$$A^{*}_{qq} = A^{*,UN}_{qq} + h_{B} \qquad , \qquad q = 1 \text{ and } N$$

$$B^{*}_{q} = B^{*,UN}_{q} + h_{B}\theta_{amb} \qquad , \qquad q = 1 \text{ and } N \quad . \qquad \text{A. 7}$$

The adiabatic boundary condition at $x = L$ (Eq.11) is recovered by setting $h_{B} = 0$. The adiabatic boundary condition at $x = 0$ has been accounted for in the above derivations.

2. Calculation of free convection coefficient h_{L}

The convective coefficient h_{L} is evaluated based on the *Nusselt number Nu* [Shu, Lagoudas,Hughes and Wen, 1997] which is given in terms of the *Rayleigh number Ra*. The thin wire is taken as a horizontal cylinder and the corresponding *Grashof number Gr* and *Prandl number Pr* is calculated from [Morgan,1975, Churchill and Chu,1975]

$$G_{r} = \left(\frac{2(\theta - \theta_{amb})}{\theta + \theta_{amb}}\right)\frac{gr^{3}}{8v^{2}} \qquad , \qquad \text{A. 8}$$

and

$$P_{r} = \frac{\mu C_{v}}{k} \qquad . \qquad \text{A. 9}$$

where $g = 9.8 \text{ m s}^{-2}$ is the acceleration due to gravity, v is kinematic viscosity, C_{v} is the heat capacity, μ is the viscosity, and k is the thermal conductivity of the surrounding air,

respectively. All the physical properties are calculated at the average temperature $\theta_{avg} =$ $(\theta + \theta_{amb})/2$. From the above the *Rayleigh number Ra* can be calculated as $Ra = G_r P_r$, and the corresponding *Nusselt number Nu* is given as [Kakac et al.,1987, Kreith and Black,1980]

$$Nu = \left[\alpha_1 + \alpha_2 \left\{ \frac{G_r P_r}{\left[1 + (0.56/P_r)^{9/16} \right]^{16/9}} \right\}^{1/6} \right]^2 \qquad \text{A. 10}$$

The constants α_1 and α_2 are given as $\alpha_1 = 1.00$ and $\alpha_2 = 0.287$ [Shu et al.,1997]. Note that there are several factors that influence the accurate evaluation of these constants, in particular electrical resistivity ρ_E. The free convective coefficient h_L is obtained from

$$h_L = \frac{KNu}{2r} \qquad \text{A. 11}$$

where K is the thermal conductivity of the given wire specimen and r is the radius.

3. Constants Z, A, C_m and λ_m as given in Eq.3-4 and Eq.3-5

$$Z = \frac{h_B}{k\sqrt{A}} \left[\frac{h_B}{k\sqrt{A}} \left(e^{L\sqrt{A}} + e^{-L\sqrt{A}} \right) + \left(e^{L\sqrt{A}} - e^{-L\sqrt{A}} \right) \right]^{-1}$$

$$C_m = \frac{Z\left[\dfrac{\sqrt{A}\ \cos(\lambda_m L)}{A + \lambda_m^2}\left(e^{\sqrt{A}\,L} - e^{-\sqrt{A}\,L}\right) + \dfrac{\lambda_m \sin(\lambda_m L)}{A + \lambda_m^2}\left(e^{\sqrt{A}\,L} - e^{-\sqrt{A}\,L}\right)\right] - \dfrac{\sin(\lambda_m L)}{\lambda_m}}{\left[L + \dfrac{\sin(\lambda_m L)}{2\lambda_m}\right]}$$

where λ_m is given by the transcendental equation

$$\lambda_m \sin(\lambda_m L) = \frac{h_B}{k}\cos(\lambda_m L)$$

and $\qquad A = \dfrac{2h_c}{rk}$

APPENDIX B

1. Calibration of the thermocouples

The calibration of thermocouples (Type J Iron-Constantan) was done using a calibrated Fluke 2180A rtd digital thermometer (with a resolution of $\pm$ 0.01 ^{0}C). Two "constant" temperature sources were used: (1) an ice-bath and (2) a water-bath measured at room temperature. The temperature of the former (θ_{ice}) as measured by the digital thermometer was found to be in the range $0 \le \theta_{ice} \le 0.05$ ^{0}C. The temperature of the water bath (θ_{water}) was measured to be $\theta_{water} = 19.5$ ^{0}C: the tolerance in measured temperature was determined to be ± 0.15 ^{0}C. The two tips of the thermocouple were first immersed in the ice-bath to find the 'zero'. The next step was to immerse one tip in the water-bath. The voltage due to the temperature differential was measured at 1.0134 mV. According to the manufacturer's (Omega) recommendation, the voltage - temperature conversion formula used was

$$\theta = 19.78425 \times v - 0.2001204 \times v^2 \qquad \text{A. 12}$$

where 'v' is the measured voltage in millivolts and 'θ' is in deg C; for $v = 1.0134$ mV, we have $\theta = 19.84$ ^{0}C. In comparison with the mean temperature of 19.5 ^{0}C measured by the digital thermometer, the error in the thermocouple is found to be 0.34 ^{0}C. This is well within the error range of ± 0.75 ^{0}C suggested by the manufacturer. The procedure of attaching the thermocouple on the SMA wire is now described.

The thermocouple was attached to the SMA using a thermal cycling adhesive under a microscope providing a magnification of 30. This was done to minimize the amount of

adhesive used so that it does not act as a heat sink during measurement while also ensuring a proper contact of the thermocouple with the wire. All the wires leading in and out of the apparatus related with temperature measurement were shielded and grounded so that induced voltage errors due to noise and electro-magnetic waves are eliminated.

2. Calibration of the voltage measuring devices

The chief voltage-measuring devices used in our set of experiments described in this dessertation are 1) The A/D boards (DAS 800 and DAS 1700 series, 2) The strip chart recorders and 3) The LVDT, oscilloscope and multimeters used in measurement of voltage and applied current.

The calibration reference for all these voltage-measuring devices was done using a fluke 343A DC voltage calibrator with a resolution of $\pm 5\mu V$. A known voltage of 0.00 volts and the other extreme of any given range (e.g. 5 mV for thermocouple and 1 V for the A/D boards, multimeters and oscilloscope) was used for this purpose. The A/D conversions of the measured data were done using two different boards on a 486 computer. A schematic diagram of the A/D calibration utilities on the DAS 1700 board is given in Fig.A-1. The calibration of the boards were done using software provided by the manufacturer and the FLUKE voltage calibrator was used for testing and verification of results. The DAS 1700 series boards were linked with a STU 1800 U screw terminal accessory and the signals were connected in a differential input configuration to reduce performance degradation. All wires leading in and out of the experimental setup was shielded to reduce noise and induced voltage pickup. All connections were sealed

together to avoid bi-metallic junctions in the input circuitry. Software filtering was provided where ever necessary by averaging readings to reduce gaussian noise.

The calibration of the strip chart recorders was also done using the FLUKE calibrator where a known voltage was used to arrive at the preferred accuracy of the equipment. The LVDT was calibrated using a screw gauge along with the calibrated A/D board. Although the calibration of the LVDT yielded a linear relationship between voltage and distance, the measurements were kept within the nominal range of the equipment so that linearity is preserved. A schematic graph showing the core position and the linear range is given in Fig.A-2.

3. Calibration of the Differential Scanning Calorimeter

The in-house INSTRUMENTS SPECIALIST INC; DSC-550 connected to a 486 computer and monitored by (TA - PC AQUIRE) software supplied by the manufacturer was calibrated using an Indium sample also supplied by the manufacturer. The transition temperature of the given indium sample starts precisely at 156.6 ^{0}C which can be used a s a reference to determine the accuracy of the DSC. The DSC is run exactly in the same manner as for the experiments with a indium sample of weight 10.2 milligrams, except that the TA-PC AQUIRE software is run with a No-Calibration option. The resulting thermogram is studied to determine the transition start temperature of the given sample. The transition temperature in our calibration trials as read from the thermogram was always within an accuracy of ±0.3 ^{0}C. A sample thermogram showing the DSC calibration run is shown in Fig.A-3.
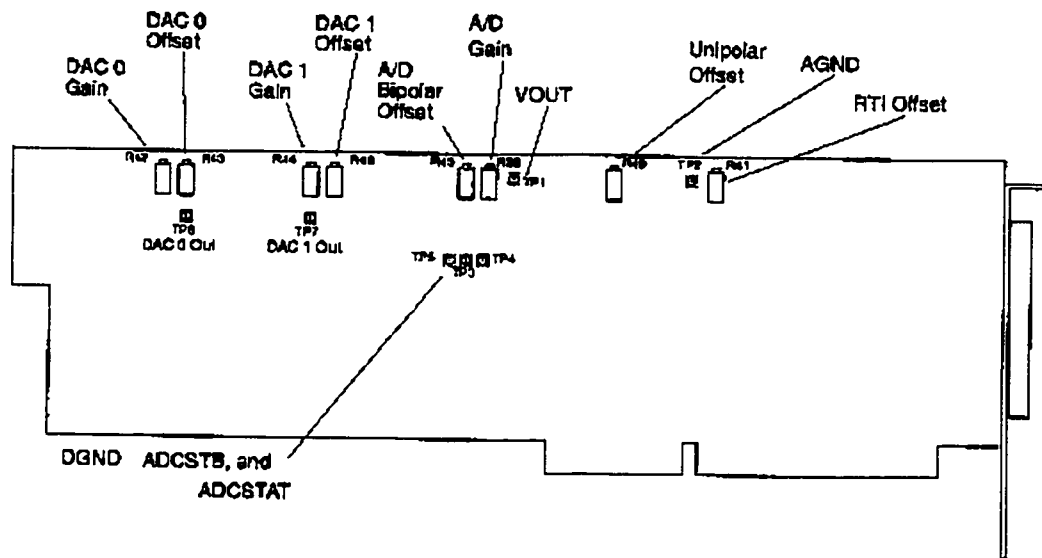
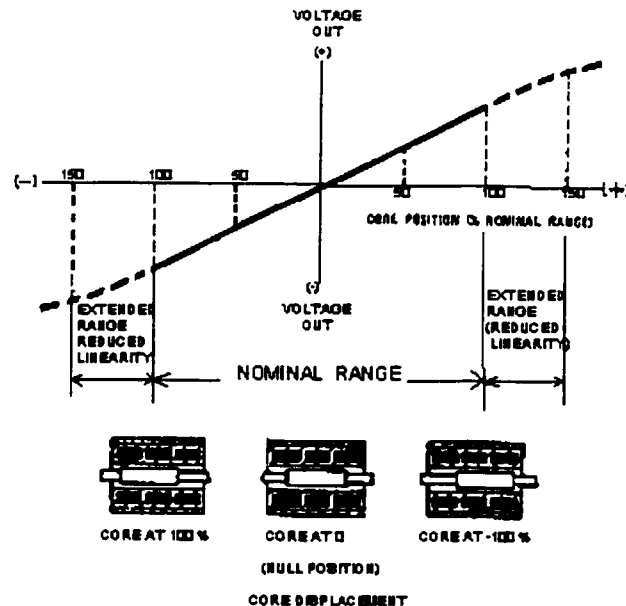Figure.A-1 Figure showing various calibration utilities on the DAS-1701 A/D board.

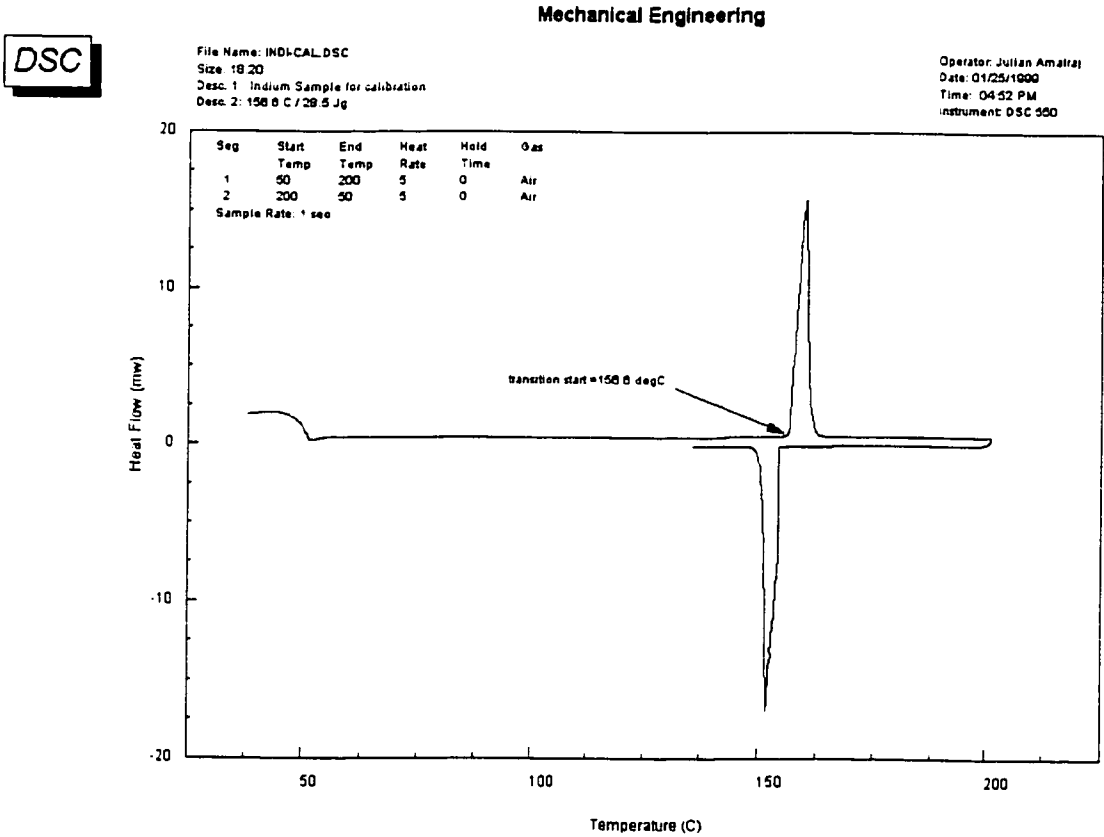Figure.A-2 Figure showing LVDT output as a function of core position.

Figure.A-3. Thermogram showing the calibration of DSC using an indium sample as

reference.